THE OBSERVED CHAOTIC ROTATION OF HYPERION

by

James Jay Klavetter

Submitted to the Department of
Earth, Atmospheric, and Planetary Sciences
in partial fulfillment of the requirements
for the degree of

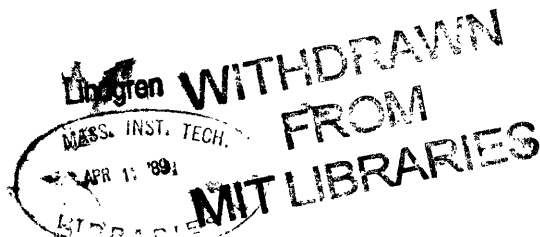Doctor of Science

at the
Massachusetts Institute of Technology

January 1989

Signature of Author_____

_____
Department of Earth, Atmospheric, and Planetary Sciences

Certified by_____

Dr. Edward Dunham
Principal Research Scientist, Department of Earth, Atmospheric, and Planetary Sciences
Thesis Supervisor

Certified by_____

Dr. James L. Elliot
Professor, Departments of Earth, Atmospheric, and Planetary Sciences and Physics
Thesis Supervisor

Accepted by__

_____
Dr. Thomas H. Jordan
Chair, Departmental Committee on Graduate Students

The Observed Chaotic Rotation of Hyperion

by

James Jay Klavetter

Submitted to the Department of Earth, Atmospheric
and Planetary Sciences on January 26, 1989 in
partial fulfillment of the requirements for the
Degree of Doctor of Science in
Planetary Science

ABSTRACT

Wisdom, Peale, and Mignard (1984) predicted Hyperion to be in a state of chaotic rotation. Simulations indicate that very precise and well-sampled observations over a few orbit periods are necessary to test this prediction (Peale 1986). I have obtained such a data set by observing Hyperion for 13 weeks (4.5 orbit periods) at observatories in Chile and in Arizona using a CCD camera.

Hyperion was observed to have an opposition surge of approximately 0.3 magnitudes at solar phase angles less than 0.3°. The R mean opposition magnitude of Hyperion is approximately 13.81, but imprecisely determined due to the unknown aspect of the satellite. The V–R color of Hyperion is 0.41 ± 0.02 magnitudes. Hyperion varies less than 0.01 magnitudes on timescales of 6 hours, thus ruling out short rotation periods.

Phase-Dispersion Minimization analysis of the resulting lightcurve definitively shows that Hyperion is not in any periodic rotation state, thus implying it is chaotic. I therefore extended the original dynamical model of Wisdom *et al.* (1984) to include all the necessary modifications to allow me to fit to my lightcurve. Numerical simulations indicate the best method used in fitting is 1) choose a well-sampled section of the lightcurve to search for and find the area in phase space that approximates the best initial condition, and then 2) fit using some minimization technique to this section, add the next observation point, fit again, and so on until the entire lightcurve is fit.

I conducted such a search and fitting procedure, marginally sampling the necessary phase space. My best fit has residuals that compare well with the internal uncertainties of the data. The moment ratios fitted compare well with those predicted from the *Voyager*-derived shape and are consistent with the satellite having a uniform density distribution.

CONTENTS

Tables

ACKNOWLEDGEMENTS

First and foremost I thank Dave Jewitt. This project would not have been done well without his help. He helped me obtain telescope time, provided financial assistance, and taught me many things.

My warmest thanks extend to Ted Dunham. He has always been available, seemingly as much as if I were one of his own children. Whether it is hardware, software, or otherware, Ted always had some insight. Or at least he took the time to think about it.

Jim Elliot has been helpful since I first met him in his observing class. If he had done nothing more than teach me the value of finishing that would have been enough.

Without Jack Wisdom, this project would have never begun. In addition to all his help and useful discussion, he helped me look at things a different way than most of the other scientists I have known. He was also indispensable for suggestions concerning my numerical simulations and for providing access to computer time.

Thanks to Dick French. In addition to another person who always made time for me, gave me his full attention, and was usually able to help me, he was able to go beyond the computer console. I will never forget January 1988. Thanks Dick.

Linda French has also become a good friend and I thank her for all her support over the years.

Special thanks goes out to my past and present office mates for putting up with me and my friends, especially the furry ones (that's the friends, not the mates). Amanda Bosh provided me with warmth, humor, and even food every once in a while. Eliot Young was an indefatigable Mac helper.

I thank all of the people who gave me technical support, especially Matt Johns, Bob Barr and Larry Bruer at MHO, Jeanette Barnes, Suzanne Jacoby, and Ed Anderson at NOAO, and the support personnel at Kitt Peak (especially the volleyball players). John Kruper and Mark Bautz both provided me with some precious telescope time.

Mom and Dad did not always understand what I was doing, or why, but they never gave up on me. It was only recently that I came to realize the magnitude of their sacrifices, support, and patience. Thanks.

The rest of my family, Mary, Elmer, and Floyd were able to help me out innumerable times and all of them did so without flinching. Special thanks to Elmer and Karen. You don't know how much you helped out just by being there.

If the manuscript is readable and if the figures look good, some of the credit goes to Anita Killian and Amanda Bosh. Anita has been a good buddy for a number of years now and I hope for more in the future.

And for those who are about as far away from Planetary Science as possible, thank you John Swomley and Jennifer Roberts. Thanks to Meredith Thomas, Roger Eichler, Mike Ames, Mark Griffith, Marc Spehlmann, Lisa Greeber, Lois Epstein, Tom Consi, and Corky Binggeli.

For all the pizza and late night discussions, Deepto Chakrabarty is someone to count on. Thank you Steve Levine and Greg Aldering for the support throughout.

For those who know me, they will understand that my deepest affection extends to my two most faithful companions, Athabasca and Reudi. They were always there and always ready for anything. A person could not ask for two better friends.

And to Eek, I wish you could have been around for a while longer.

I . INTRODUCTION

Hyperion (SVII) is unique in the solar system. This satellite of Saturn is the only major body presently rotating chaotically, as demonstrated by this work. In most respects, however, it is an unremarkable object. Hyperion's orbit has a semimajor axis of 24.6 Saturn radii, a period of 21.3 days, and an inclination of 0.43°. A 4:3 orbital resonance with Titan forces the orbit of Hyperion to remain at a relatively large mean eccentricity of 0.1042. The best pre-*Voyager* radius, determined radiometrically, was 140 ± 19 km and the visual geometric albedo was determined to be 0.28 ± 0.04 (Cruikshank and Brown 1982). *Voyager* images revealed the irregular shape of Hyperion, which has approximate dimensions of $185 \times 140 \times 113 \pm 10$ km (Thomas and Veverka 1985). Hyperion is the most irregularly shaped of the major satellites. This, in conjunction with the large forced eccentricity, led Wisdom *et al.* (1984) to predict that Hyperion would be in a rotation state of chaotic tumbling. This chaotic rotation state has now been conclusively confirmed with my observations taken during the summer of 1987 and subsequent analysis and modeling.

The rest of this section will provide some necessary background, including previous observational attempts to determine Hyperion's rotation state, and *Voyager* results. In Section II, I will discuss the theory necessary to understand the chaos arising from the spin-orbit coupling in the Hyperion-Saturn system. The dynamics covered in Section II are results from investigations by Wisdom *et al.* (1984) and provide the theoretical framework for this work. I observed Hyperion at three sites over an interval of three months, discussed in Section III. In Section IV I will explain the procedures used to produce my lightcurve, the reduction of which was complicated by a background light gradient and a large number of background stars. Section V outlines the different methods used to analyze Hyperion's rotation state and fully developes the dynamical model used in the fits to my lightcurve. I will discuss the results and consequences of this research in Section VI. The final section lists my conclusions.

Familiarity with the observations of and theories concerning Hyperion is necessary to understand the dynamical questions associated with this satellite. After briefly describing theories of Hyperion's formation and its surface composition, I will review the previous observational studies of Hyperion, with special attention to those that attempted to determine its rotation state. *Voyager* observations will then be discussed. Table I is a listing of Hyperion's physical characteristics.

Table I. Physical Properties of Hyperion

Property	Value	Reference
radius	185 x 140 x 113 ± 10 km	Thomas and Veverka 1985
mass	unknown	
density	unknown	
geometric albedo	0.19 – 0.25	Tholen and Zellner 1983
surface composition	dirty ice	Clark et al. 1984
semimajor axis	24.55 R_s	Woltjer 1928
Distance from Saturn in 1987:		
maximum at elongation	239 arcsec	
minimum at conjunction	86 arcsec	
orbital period	21.277 days	Woltjer 1928
rotational period	chaotic	Wisdom et al. 1984, Klavetter 1989
eccentricity	0.1042 (forced)	Woltjer 1928
inclination	0.43°	Woltjer 1928
V_o	≈ 14.2	(see Table III)
B – V	≈ 0.74	(see Table III)
V – R	0.41 ± 0.02	Klavetter 1989
J	13.0 ± 0.10	Cruikshank 1979
J – H	0.15 ± 0.05	Cruikshank 1979
J – K	-0.03 ± 0.07	Cruikshank 1979
J – L	>0.55	Cruikshank 1979
lightcurve amplitude	≈ 0.5	Thomas and Veverka 1985

Since Hyperion has such an aspherical shape, it is natural to ask how it could have obtained this shape. No other large satellite has such an odd shape. Mimas, for example, is about the same size as Hyperion yet is well approximated by a nearly spherical ellipsoid. It is difficult to determine the relative importance that fragmentation processes and tidal/gravitational forces have had in shaping Hyperion due to a lack of information concerning collisions and material strengths. Smith et al. (1981) proposed a model in which collisional fragmentation and reaccretion, perhaps even multiple collisions and reaccretions, account for many of the observed characteristics of the Saturnian satellites.

Thomas *et al.* (1983) stated that it was unnecessary to invoke such a "spectacular" explanation for the origins of many of the Saturnian satellites. They noted that cratering statistics indicate that any fragmentation and reaccretion must have occurred at least a few billion years ago based on the crater counts observed. Farinella *et al.* (1983) proposed a model in which Hyperion is the "core" of a disrupted predecessor. Their calculations indicate that the 4:3 orbital resonance with Titan would prevent any reaccretion of secondary fragments, which would either fall into Titan or would escape from the Saturn system. While the origin of Hyperion is an interesting question, I will deal with the consequences of Hyperion's shape rather than how it was formed.

The inner satellites of Saturn are mostly ice, as conclusively demonstrated by *Voyager* determination of masses and radii which showed that their densities were of the same order as water-ice (Smith *et al.* 1982). Unfortunately, there is no good mass determination of Hyperion. In principle, a mass could be computed from consideration of the 4:3 Titan-Hyperion orbit-orbit resonance, but Titan is so much more massive than Hyperion that this is impractical. Cruikshank and Brown (1982) calculated a geometric albedo of $p_v = 0.28 \pm 0.04$ for a Hyperion with an effective radius of 140 ± 19 km. This is consistent with the value found by Tholen and Zellner (1983) of 0.19-0.25. The range of values is given since they did not know the aspect of the satellite. These values are similar to those found for some asteroids and rocky bodies, but typically less than most icy satellites. Infrared measurements in the region $1.5 - 2.6$ μm by Cruikshank and Brown (1982) and Clark *et al.* (1984), however, strongly indicate the presence of water-ice on Hyperion's surface. It is unknown if water-ice is a major constituent of Hyperion's bulk composition or if water-ice is just a part of a dirty-frost regolith. Chapman and McKinnon (1986) argued that central peaks would not be found in the largest craters if Hyperion were silicate due to the greater effective strength of cratered rock debris compared to ice. Since they reported finding central peaks in such craters, they believe Hyperion to be an icy satellite. Cruikshank *et al.* (1983) proposed a model in which Phoebe, or some other outer Saturnian body, "hails" dust down to Iapetus and Hyperion. This scenario would not constrain the composition but it could account for Hyperion's relatively low albedo if an icy composition is assumed. Although the colors of the leading (dark) side of Iapetus and Hyperion are similar, Tholen and Zellner (1983) have shown that the broadband colors of Hyperion and Phoebe differ significantly. While this is an interesting area of research, the surface characteristics or bulk composition of Hyperion will not directly affect the dynamics. It will be shown, however, that the principal moments of inertia can be constrained using dynamical considerations. Thus it is important to consider how different compositional stratifications could affect the moments and the dynamics.

The rotation state of Hyperion can be examined using well-sampled, precise, ground-based observations. Assuming Hyperion's rotation is chaotic, all data sets prior to this work are undersampled, as established by Peale (1986), Wisdom and Peale (1984), and Wisdom *et al.* (1984). This is because the traditional technique of folding the data set back upon itself and applying least-squares analysis can produce results that can appear quasiperiodic for chaotic rotation states. Table II lists the attempts to resolve Hyperion's rotation state using observational data.

Table II. Hyperion Rotation Data Sets

Observer	Δm^a	N^b	T^c	Comments
Andersson (1974)	0.10	13	742	Used aperture photometer, omitted 2 observations.
Goguen *et al.* (1983)	0.48	18	160	Used aperture photometer.
Conner (1984)	0.51	8	20	M.S. Thesis, M.I.T.
Klavetter (1985)	0.45	16	40	Unpublished.
Thomas and Veverka (1985)	0.52	14	61	*Voyager* data.
Binzel *et al.*(1986)	1.10	8	15	No sky gradient fitting.
Klavetter (1989)	0.53^d	37	53	38 total observations: one 11 days after main data.

a   Lightcurve amplitude.
b   Total number of nights observed.
c   Total time interval of the observations in days.
d   Omitting observations near opposition surge.

Andersson (1974) and Goguen *et al.* (1983) used aperture photometers (photomultipliers that give an integrated number of counts for the entire aperture). It is very difficult to accurately subtract the background with aperture photometers due to the nonlinear background light gradient from nearby Saturn, as will be demonstrated in Section III. Andersson (1974) presented 13 data points observed over a 742 day interval. After disregarding two of the observations, he presented a lightcurve "[consistent] with the satellite's brightness being constant." He concluded that Hyperion's magnitude was probably constant or possibly variable at the 0.1 magnitude level. Andersson did not know of *Voyager 2* results and disregarded two data points as being anomalous. Since his observations were taken with an aperture photometer and were grossly undersampled, Andersson's observations place no constraint on Hyperion's rotation state.

Goguen *et al.* (1983) observed Hyperion for 18 nights over a 160 day interval. They folded back the lightcurve, performed a least-squares analysis and found a 13 day period. However, the fit of this period to this data is not good: observations at identical phase differ by one-half the total amplitude, "many times the measurement error" (Goguen, personal communication 1986). These observations were taken with an aperture photometer and were undersampled as well.

Conner (1984) was the first to demonstrate the feasibility and importance of background gradient subtraction with a CCD, but his data are also undersampled with only 8 observations in a 20 day interval. Klavetter (1985, unpublished), with 16 observations over a 40 day interval, is another undersampled data set which is inconclusive.

Thomas and Veverka (1985) analyzed *Voyager* observations taken over an interval of 61 days. In their first paper (Thomas *et al.* 1984), using 14 low-resolution images and traditional techniques of folding back the lightcurve and least-squares analysis, they reported Hyperion to be in a "coherent 13.1-day spin over [a time interval of] 61 days," with the spin axis nearly parallel to the orbital plane. They stated that this is an "unusual" spin state, consistent with chaotic rotation. Further analysis (Thomas and Veverka 1985) took advantage of the high resolution images but could not match landmarks using the 13.1 day period: "the net rotation during this time [61 days] is uncertain by 50%."

Binzel *et al.* (1986) presented a lightcurve of 8 observations over a time period of 15 days. It is a lightcurve with an amplitude of 1.10 magnitudes, twice the amplitude as measured by any other observer. Based on *Voyager* images, shape and albedo variations should produce a lightcurve amplitude of 0.4 to 0.5 magnitudes (Thomas and Veverka 1985). Binzel *et al.* (1986) did not directly mask the light from Saturn or perform any background sky gradient fitting and subtraction. Since their anomalous data points were observed near the time of conjunction with Saturn, this probably explains their unusually large magnitude amplitude.

Although observations adequate to determine synchronous or periodic rotation states of Hyperion have been attempted, all previous data sets are inadequate to resolve Hyperion's rotation state unambiguously. All data sets are undersampled and some have uncertainties due to the background light gradient.

Table III lists the previous measurements of Hyperion's photometric properties. There is general agreement among observers, especially since all measurements strongly depend upon the aspect of the satellite, which no observer knew at the time of the

observations. The mean opposition magnitude of Hyperion is $V_o \approx 14.3$ with colors of $B - V \approx 0.74$ and $V - R = 0.41 \pm 0.02$ (see Section IV). In addition, Cruikshank (1979) reports the infrared colors listed in Table I. Even when an observer takes great care to eliminate any systematic errors and follows a proper data reduction procedure, caution must be used in interpreting the data. Due to the large lightcurve amplitude and the seemingly random nature of chaos, it is possible to unintentionally observe Hyperion preferentially when it is brighter, for example, than its mean opposition magnitude unless it is sampled nearly every night. Another effect not known until recently, the opposition spike (Klavetter 1989), is exemplified by the observations of Franklin and Cook (1974). They report a mean opposition magnitude significantly brighter than all other observers, but both of their observations were made near opposition, at solar phase angles $\alpha \leq 0.3°$. This is the expected effect of the opposition surge, however, so that these observations, corrected for the phase effect, are consistent with the others. Thus, any discrepancies in the photometric properties listed in Table III may be due, in part, to the nature of Hyperion's rotation state.

Table III. Hyperion's Photometric Properties

Observer	V_o[a]	B-V	β[b]	Δm[c]	N[d]
Harris (1961)	14.16	0.69	----	----	5
Andersson (1974)	14.16	0.78	0.025	0.10	13
Franklin and Cook (1974)	13.93[e]	----	----	----	2
Degewij et al. (1980)	14.18	0.77	0.380[f]	0.36	12
Goguen et al. (1983)	14.20	----	0.037	0.48	18
Tholen and Zellner (1983)	14.36	0.73	----	----	2
Conner (1984)	14.82	0.69	----	0.51	8
Klavetter (1985)	14.42	0.77	----	0.45	16
Thomas and Veverka (1985)[g]	----	----	≥0.018	0.52	14
Binzel et al.(1986)	14.42	----	----	1.10	8
Klavetter (1988)	14.23	----	0.056[h]	0.53	38

a   Mean opposition magnitude.
b   Linear phase coefficient.
c   Lightcurve amplitude.
d   Total number of nights observed.
e   Both observations at ≤0.3° solar phase angle.
f   This is an "adopted value" for all outer solar system objects and not measured for Hyperion.
g   *Voyager* observations.
h   Not including opposition surge.

The *Voyager* spacecraft provided a wealth of new information concerning Hyperion. The *Voyager 2* determination of the shape of Hyperion directly led to the prediction of its chaotic rotation (Wisdom *et al.* 1984). Unfortunately, only about 50% of Hyperion was observed by *Voyager* at high resolution (Thomas and Veverka 1985) so the shape is still uncertain and it is impossible to map the surface of Hyperion with the topographic features observed. The following results are reported by Thomas and Veverka (1985). Although Hyperion's shape is not precisely ellipsoidal, the best determined dimensions are 185 x 140 x 113 ± 10 km. Hyperion's average normal reflectance is 0.21 at 0.47μm and any variations in albedo are essentially averaged out over the disk. Its color is redder than Phoebe but is nearly the same as the dark (leading) side of Iapetus. While there are identifiable craters, the crater density is low compared to the other Saturnian satellites. Figure 1 is the highest resolution image of Hyperion taken by *Voyager 2*. This figure clearly shows Hyperion's highly aspherical shape that can roughly be described as ellipsoidal. Unfortunately, the *Voyager* spacecraft were not able to constrain Hyperion's mass. While only about one-half of the surface was imaged at high resolution, *Voyager* roughly determined Hyperion's shape, leading to investigations of its dynamics. *Voyager* was not able to independently determine the principal moments of inertia, but these can be calculated if a uniform density is assumed.

As will be seen in the next section, Hyperion's odd shape is important to its dynamics. Yet, it is still uncertain exactly how such a large object could form into such a shape. While it seems unlikely that gravitational or tidal forces alone could account for Hyperion's shape, it is uncertain to what extent collisional fragmentation and reaccretion contributed to Hyperion's origin. Its formation might be better constrained if the composition of Hyperion were known, but unfortunately there is no good mass determination of Hyperion and thus no constraint on Hyperion's density. Its albedo is more indicative of a rocky type of surface, unlike most Saturnian satellites. It is possible, however, that the surface has been contaminated from dust originating from a Phoebe-like object so as to darken its surface. Water-ice has been detected from Hyperion's surface but it is not known if this is a major constituent. Given the shape, whatever the origin and composition, the questions concerning Hyperion's dynamics have eluded observers since Hyperion was first observed. All observations until this work were too undersampled to determine or constrain Hyperion's rotation state. With some observations, there was the problem of subtracting a highly nonlinear background light gradient. There has been some disagreement between observers concerning Hyperion's brightness and colors, some of which could be due to the rotational state of Hyperion. Fortunately the *Voyager 2* spacecraft provided some data concerning Hyperion, including its albedo and shape. It is

the shape determination which led Wisdom *et al.* (1984) to predict Hyperion to be in a chaotic rotation state. This prediction will be the topic of the next section.
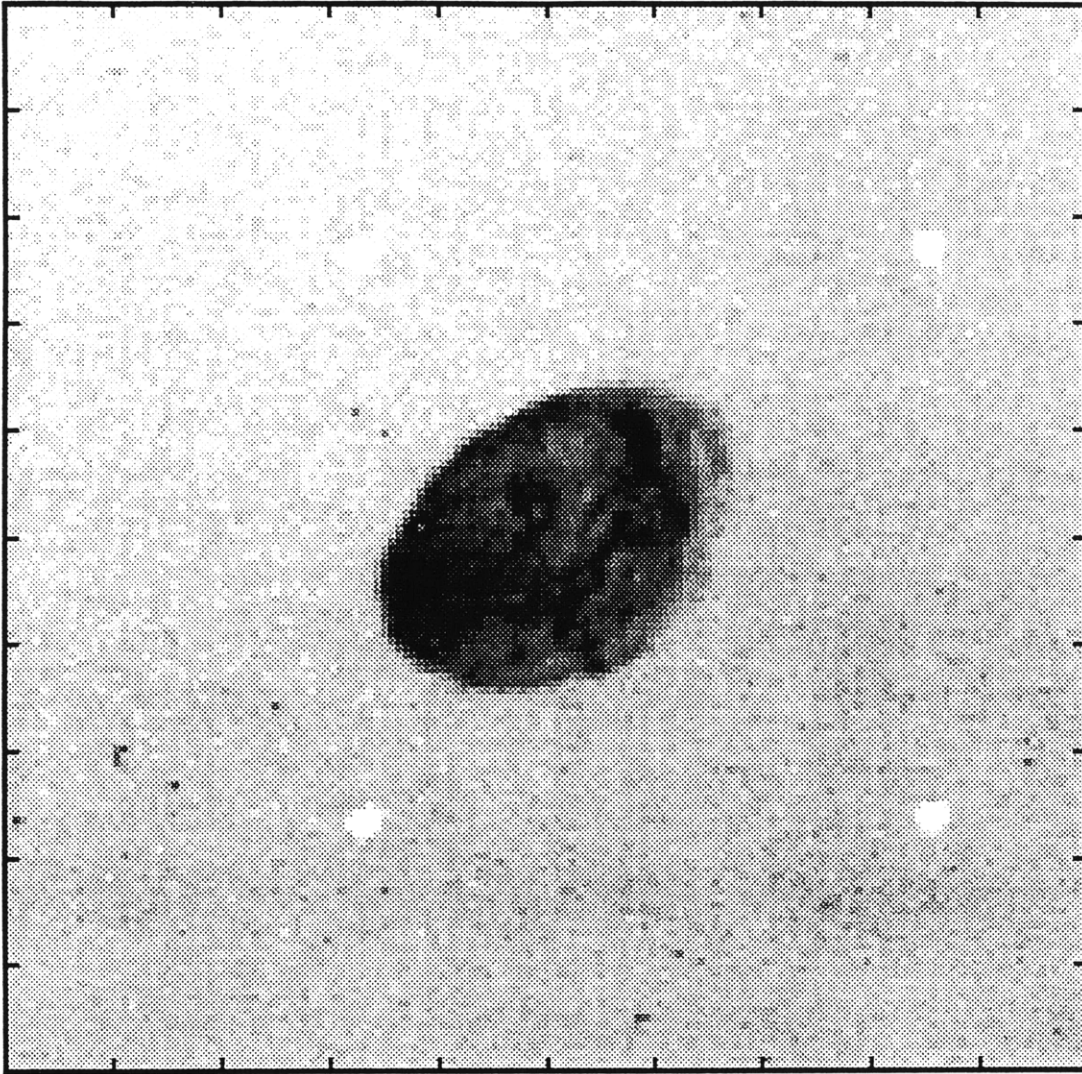

Figure 1.   One of the highest resolution images of Hyperion. The terminator is to the right in this picture. Note that the outline is closely approximated by an ellipse. Even though this is a high resolution image of Hyperion, surface features are difficult to distinguish. The albedo is approximately constant between different sections of the surface.

II . DYNAMICS

Chaotic motion is deterministic but unpredictable motion due to exponential divergence of nearby initial conditions (Hénon and Heiles 1964; Wisdom 1987). Chaos is not random, it is deterministic. This apparent contradiction will be resolved in this section. I will review the work of Wisdom *et al.* (1984) and discuss the theoretical prediction of Hyperion's chaotic rotation. Various definitions and explanations will be presented which will be used in the analysis and fitting of the lightcurve (Section V).

Until recently, Mercury was the only object in the solar system known to have a commensurate yet nonsynchronous spin rate. Goldreich and Peale (1966) discussed spin-orbit coupling in the solar system and the capture probability of an object evolving into resonance due to tides. They derived a pendulum-like equation for spin-orbit coupling states by averaging nonresonant terms over an orbit period. Wisdom *et al.* (1984) demonstrated that this averaging technique is not applicable when the width of the resonance is a large feature of phase space. The width of the resonance increases with ω_0 where $\omega_0^2 \equiv 3(B - A)/C$ and $A < B < C$ are the principal moments of inertia. ω_0 is a quantity that increases as a uniform body becomes less spherical. Thus, as a uniform body becomes more ellipsoidal, the widths of the resonances get large.

If the widths of the resonances get too large, their chaotic separatrices will begin to overlap. Physically, this means that a body would apparently be in two rotation states at the same time, such as rotating synchronously and in the 3:2 state simultaneously. Since it is impossible for a body to be in two resonances at once, chaotic behavior is the result when this overlap occurs. The approximate point at which this happens is given by the Chirikov resonance overlap criterion (Chirikov 1979). Considering the synchronous and 3:2 states, the Chirikov overlap criterion is

$$\omega_0^{RO} = \frac{1}{2 + \sqrt{14e}} \cdot$$

At the eccentricity of Hyperion, the critical value is $\omega_0^{RO} = 0.31$. Above this value, chaotic behavior will be widespread throughout phase space. For Hyperion, $\omega_0 = 0.89 \pm 0.22$ (Duxbury, as reported by Wisdom *et al.* 1984). This is much larger than the critical value. Clearly, chaos is expected in an investigation of the rotational phase space of Hyperion.

The phase space of Hyperion can be investigated numerically. To do this, the equations of motion are needed. Following Wisdom *et al.* (1984), an ellipsoid model is used with a, b, c defining a right-handed set of axes fixed in the satellite corresponding to the principal moments of inertia A < B < C, as illustrated in Figure 2. In this case, Euler's equations are

$$A\frac{d\omega_a}{dt} - \omega_b\omega_c(B - C) = -\frac{3}{r^3}\beta\gamma(B - C),$$

$$B\frac{d\omega_b}{dt} - \omega_c\omega_a(C - A) = -\frac{3}{r^3}\gamma\alpha(C - A), \tag{1}$$

$$C\frac{d\omega_c}{dt} - \omega_a\omega_b(A - B) = -\frac{3}{r^3}\alpha\beta(A - B),$$

where ω_a, ω_b, and ω_c are the rotational angular velocities about the body axes and r is the Saturn-Hyperion distance. The angles α, β, and γ are the direction cosines with respect to the planet-to-satellite radius vector of the three body axes. Units are chosen such that the semimajor axis is one, the orbital period is 2π, and the dimensionless time is the mean anomaly. All angles are in radians and the corresponding angular velocities are in dimensionless units of rotations (2π) per revolution (2π).
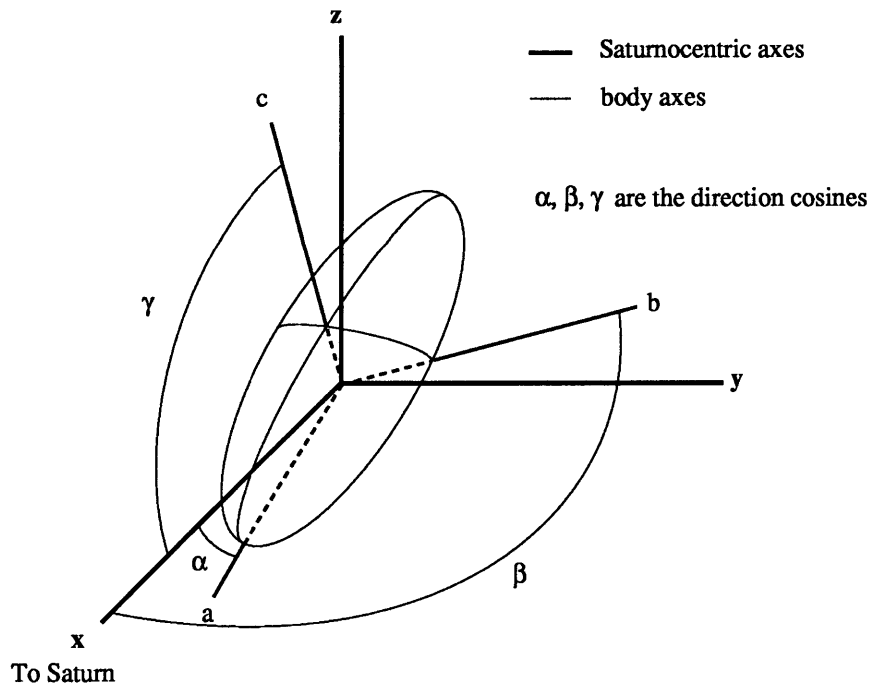

Figure 2.   Definition of the body frame, Saturnocentric (reference) frame at periapse, and direction cosines.

Two sets of generalized coordinates are necessary to solve these equations since there will be situations in which a singularity is encountered in any coordinate system and it will be necessary to switch to another coordinate system. One set of coordinates will be the usual Euler angles (Goldstein 1965). The other coordinate system will be that chosen by Wisdom *et al.*(1984) and hereafter referred to as the Wisdom coordinates. Both coordinate systems have a reference frame defined at periapse as follows: the x axis is parallel to the planet-to-satellite vector, the y axis is parallel to the orbital velocity, and the z axis is normal to the orbit plane, completing a right-handed coordinate system. See Figure 2. The three rotations defining the Euler angles, as illustrated in Figure 3, are defined by the following rotations. First, the body axes are rotated about the z axis by an angle θ. Next is a rotation about the new x axis, the x' axis in Figure 3, by an angle φ. The third rotation is about the new z axis, which is the c axis, by an angle ψ. The transformation from the Saturnocentric axes to the body axes using the Euler angles is derived in Appendix A. The Wisdom coordinate system differs in the third rotation ψ^w, which is about the new y axis. In either coordinate system, the rotations θ, φ and ψ describe the spatial orientation of the ellipsoid.
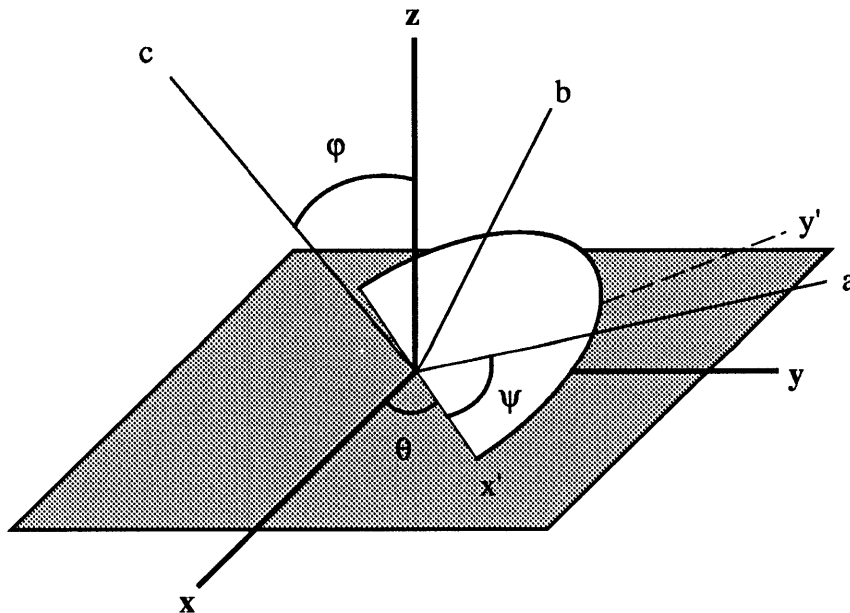

Figure 3.   The rotations defining the Euler angles. The axes are labelled as in Figure 2.

I will derive the equations of motion for the Euler coordinates. Wisdom *et al.* (1984) outline the derivation of the equations of motion for the Wisdom coordinates. The components of the angular velocities about the body axes in Euler coordinates are (see appendix B)

$$\omega_a = \dot{\theta} \sin \varphi \sin \psi + \dot{\varphi} \cos \psi$$

$$\omega_b = \dot{\theta} \sin \varphi \cos \psi - \dot{\varphi} \sin \psi \qquad (2)$$

$$\omega_c = \dot{\theta} \cos \varphi + \dot{\psi}$$

where a dot over the angle represents differentiation with respect to time.

The direction cosines are (see Appendix C)

$$\alpha = \cos(\theta - f)\cos \psi - \sin(\theta - f)\cos \varphi \sin \psi$$

$$\beta = -\cos(\theta - f)\sin \psi - \sin(\theta - f)\cos \varphi \cos \psi \qquad (3)$$

$$\gamma = \sin(\theta - f)\sin \varphi$$

where f is the true anomaly of the satellite. The equations of motion are derived by differentiating equation (2) with respect to time and substituting equations (1) and (3) into the new second order equations. These are then the equations of motion. The details of the derivation are given in Appendix D. The variables used in the equations of motion, θ, $\dot{\theta}$, φ, $\dot{\varphi}$, ψ, and $\dot{\psi}$ are the *dynamical state variables*. These state variables, as well as two parameters related to the principal moments of inertia (see Section V), define a *rotation state*. If the rotation state is specified at a certain time, such as the true anomaly, it is known as an *initial condition*.

It has already been demonstrated using the Chirikov overlap criterion that the phase space of Hyperion's spin-orbit coupling will exhibit large scale chaos. As posed, however, the phase space is six dimensional and difficult to visualize. If the spin axis is fixed perpendicular to the orbital plane, as would be expected for a tidally evolved synchronously rotating satellite, and the corresponding angular velocity, $\dot{\theta}$, is the only nonzero component of the velocity vector, the phase space is reduced to two dimensions with explicit time dependence. With these constraints, Goldreich and Peale (1966) derive the equation of motion for θ without external torques as

$$\ddot{\theta} + \frac{\omega_0^2}{2r^3} \sin 2(\theta - f) = 0.$$

This is just a special case of the full three dimensional problem, however, with

$\varphi = \dot{\varphi} = \psi = \dot{\psi} = 0.$ The problem is now reduced to an easily visualized Poincaré plot, or surface of section, in which the angular velocity is plotted versus the orientation at every periapse passage. Wisdom *et al.* (1984) demonstrate the onset and growth of chaos as ω_0 increases. When ω_0 is as large as Hyperion's value, chaos is a major feature of phase space. Figure 4 is the surface of section appropriate for Hyperion. In a surface of section, quasiperiodic zones are identified by the individual points which lie on a well defined curve. The apparently random assemblages of points are the chaotic regions.
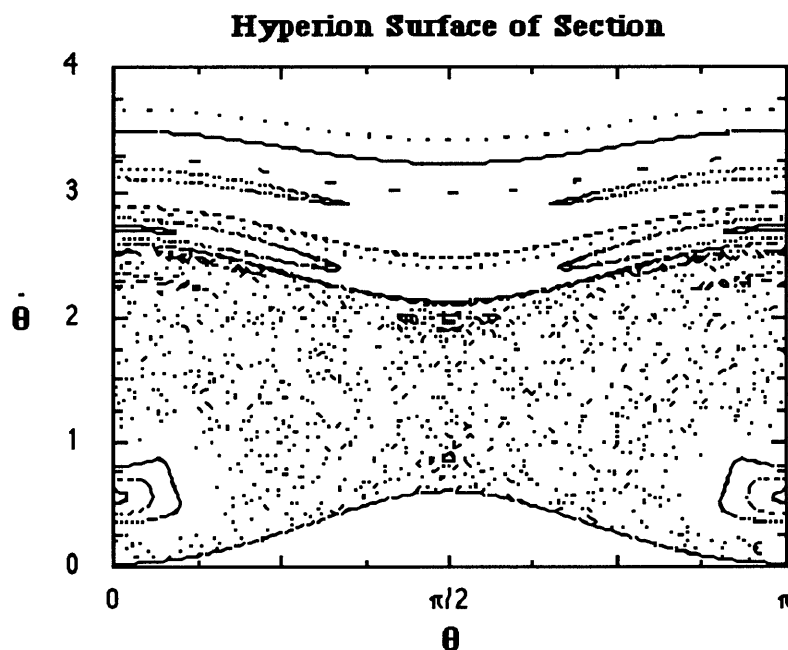
Hyperion Surface of Section

Figure 4.   Surface of Section for values appropriate for Hyperion. The equations of motion are integrated and the orientation versus spin rate is plotted at each periapse passage. Quasiperiodic areas are surrounded by points that form a nearly continuous curve. Chaotic areas are the seemingly random scatter of points. Fifteen initial conditions were integrated for 300 points each to produce this plot. The synchronous, 1:2, and 2:1 rotation states, are completely surrounded by the large chaotic zone. The 3:2 state is nonexistent.

During Hyperion's tidal evolution, the satellite is driven towards the synchronous state and inevitably ends up in the large chaotic zone seen in Figure 4. Wisdom *et al.* (1984) demonstrated that Hyperion is attitude unstable for the synchronous state and the 1:2 rotation state. That is, infinitesimal deviations of the orbital axis from the perpendicular to the orbital plane will cause further deviations which grow until the satellite starts to tumble. Only the small 9:4 and 2:1 rotation states are attitude stable. There is virtually no possibility of Hyperion entering the synchronous or 1:2 state since the chaotic zone is also attitude unstable. Capture into any other state is extremely unlikely since Hyperion must enter the state with the spin axis "randomly" oriented perpendicular to the orbital plane and

must also stay in the special configuration long enough for the weak tidal dissipation to capture the satellite into the stable rotation state. Numerical simulations support this expectation (Wisdom *et al.* 1984).

The above analysis was of a restricted model in which the spin axis was set perpendicular to the orbital plane. The evidence has clearly demonstrated Hyperion's chaotic nature, but the full equations of motion have not yet been fully explored. Fortunately, these equations can be used to predict the nature of Hyperion's rotation state using Lyapunov characteristic exponents. Lyapunov exponents measure the average rate of exponential separation of nearby trajectories (see Wisdom 1983 for a more complete discussion). A nonzero Lyapunov exponent indicates the reference trajectory is chaotic while zero exponents indicate quasiperiodic motion. Wisdom *et al.* (1984) calculate Lyapunov exponents for a number of trajectories and find them to be nonzero, indicating chaotic behavior for the Hyperion system. The Lyapunov exponents can also be a measure of the timescale for diverging initial conditions. The values found for the Hyperion system indicate that initially close rotation states widely diverge in only two orbital periods.

One important aspect of chaotic motion often ignored is the constraint put on an observer attempting to gather data on a chaotic system. Wisdom *et al.* (1984) point out that meaningful results will not be obtained if the period of the observed object varies on a time scale which is short compared to the time between the observations. If an object is rotating chaotically, it makes no sense to fold back the lightcurve to obtain meaningful results. Quasiperiodic light variations are not only possible, but common with undersampled data that is folded back and subjected to least squares analysis (Peale 1986, Peale and Wisdom 1984). Thus, the 13.1 day period derived from *Voyager* data (Thomas *et al.* 1984, Thomas and Veverka 1985) does not imply any regular rotation period since the data are undersampled (see Table II). Only with a sampling rate of about 1 observation per 1.5 days will the ambiguities be resolvable (Peale 1986, Peale and Wisdom 1984).

The model used for the study of Hyperion's chaotic rotation is an ellipsoid in a spin-orbit coupling system having the orbital characteristics of Hyperion. *Voyager* provided information on the approximate dimensions of Hyperion which were integrated into the model. The model was investigated from a purely theoretical point of view and the Chirikov overlap criterion demonstrated that Hyperion has a large chaotic region in phase space. Numerical integrations of the model in which the spin axis was set to be

perpendicular to the orbital axis confirmed this large chaotic region. Wisdom *et al.* (1984) showed the attitude instability inherent in the synchronous and 1:2 states as well as the large chaotic region. Thus, these resonant states are simply not accessible to Hyperion. Their numerical experiments demonstrated a very low probability of ever reaching any other commensurate rotation state. Finally, the full six dimensional system was investigated with Lyapunov exponents which were all nonzero confirming that this system is fully chaotic. The theoretical groundwork is well established: Hyperion should be found to be rotating chaotically. Do the observations support such a theory?

III . OBSERVATIONS

Hyperion, with an absolute R magnitude of about 14, has a large lightcurve amplitude of $\Delta R \approx 0.5$. An object of this magnitude is generally within the observational capability of a small to moderate sized telescope (diameter $\approx$ 1m) used with an aperture photometer. However, the presence of Saturn, an object almost a half a million times brighter and only 1.3 to 4 arcminutes away causes a large, nonlinear background gradient. Since numerical simulations indicated that nearly nightly sampling and a long baseline were necessary to unambiguously determine Hyperion's rotation state (Peale 1986, Wisdom and Peale 1984, Klavetter 1985, unpublished), I observed Hyperion as frequently as possible for a period of 13 weeks (91 days), typically half the night every clear night in this interval (see Table IV). My first observations were made at Cerro Tololo Interamerican Observatory (CTIO) one month before Saturn opposition. I then observed for one week at Lowell Observatory and for nine weeks at McGraw-Hill Observatory (MHO). See Table IV for a summary of the observations. The information in this section and the next can also be found in Klavetter (1989).

Table IV. Observing Sites

Observatory	Scale	Dates, 1987	Nights Allocated[a]	Nights Photometric[b]
CTIO[c] 1.0^m	16.5"/mm	05/04 - 05/17	14	8
Lowell 0.6^m	1.5"/pix	05/20 - 05/26	7	2
MHO 1.3^m	0.6"/pix	06/01 - 06/16	16	12
MHO 2.4^m	0.6"/pix	06/17 - 07/06	16	14
MHO 1.3^m	0.6"/pix	07/07 - 08/05	30	15

a   Number of nights observing time was allocated at these telescopes.
b   Number of photometric (less than 5% sky variation) nights.
c   Used aperture photometer.

At CTIO, I used the 1m telescope and the Automatic Single-Channel Aperture Photometer (ASCAP) with a 0.7mm (11.6") diameter aperture. Since there had been published observations of Hyperion made with an aperture photometer, I inferred that background subtraction would not be an insurmountable problem. This turned out not to be the case. I measured the sky using 3 different methods: 1) I moved the aperture toward, away, and perpendicular to Saturn and then averaged the 4 measurements; 2) I used an aperture that had 4 holes offset from the center allowing me to accomplish nearly

the same measurement as described in method (1) without having to move the telescope; and 3) I used an aperture that had two holes offset from the center aligned in the perpendicular direction to Saturn allowing me to measure the sky background at a number of different radial positions. Then I fit for the sky value at Hyperion's position, a procedure similar to using an area scanning photometer (as described by Franz and Millis 1971). The general observing technique and equipment were adequate to reproduce standard stars to better than 1% (1% ≈ 0.01 magnitudes), regardless of the method used to subtract the sky. Although I attempted sky subtraction around Hyperion with these three independent methods, none gave consistent results. The sky gradient was too large and nonlinear to allow accurate measurements of the sky value using the techniques explained above. Numerical simulations indicate that Hyperion observations must be accurate to within about ± 3% to be useful for model fitting. An accuracy of ± 5% is one fifth the lightcurve amplitude, and thus questionable for period fitting. Since my reduced CTIO observations of Hyperion had formal and statistical uncertainties ranging from 0.02 to 0.3 magnitudes, it was obvious that I had not achieved the required precision and thus do not include these observations. This work also demonstrates that previous aperture photometry of Hyperion may not be as precise as formal uncertainties indicated.

At Lowell Observatory I used the Mark IV TI 800x800 CCD camera on the 0.6m Morgan telescope. Cloudy observing conditions and a large image scale made the photometry noisy (see Table IV). As mentioned in the last section, accurate photometry requires good subtraction of the background sky gradient. Background subtraction is much more accurate with a more expanded scale. While sky subtractions were performed and the observations reduced to magnitudes, the uncertainties were still relatively large, 0.05 to 0.10 magnitudes. Since I only have two isolated and noisy observations from the Lowell observing run that are separated from MHO observations by nine days, I will not include these data in the analysis and avoid any systematic errors that might otherwise occur. Caution must always be taken when discarding data, but the Lowell and CTIO data were not useable for the determination of Hyperion's rotation state.

The observations from MHO are of high quality. I observed Hyperion from May 31, 1987 through August 5, 1987. Before "monsoon season" began, there were only 11 nights of non-photometric weather with most of the other nights being photometric to 1-2%, as determined from extinction curves. In addition to the non-photometric nights, I did not obtain data on three nights, one due to equipment failure, one because of high wind, and one when the diffraction spike from Titan was too close to Hyperion. As can be seen from Table II, 37 useful nights of Hyperion data were obtained over a time period of 53 days, with another observation 11 days later during the monsoons.

I observed with the 1.3m and 2.4m telescopes at MHO using focal ratios f/13.5 and f/7.5, respectively, with the MASCOT CCD (Meyer and Ricker, 1980) and the MIS (Multiple Instrument System) CCD finder/guider. On both telescopes, the scale was 0.6"/pixel. All observations were made through standard KPNO filters in the R passband, central wavelength $\lambda_0 = 634$nm and full width at half-maximum FWHM = 124nm, and V passband, $\lambda_0 = 548$nm and FWHM = 117nm. I used the R filter because the chip is most sensitive in this region of the spectrum and because the extinction is typically less in R than other passbands. V observations were made on 6 nights so that accurate color corrections could be made. To reduce the scattered light from Saturn as much as possible, a half-mirror was placed in the optical path such that the direct light from Saturn was never near the CCD chip, optics, or even the sides of the photometer box and rough black cloth was placed on all flat surfaces inside the photometer box. The MASCOT has a readout noise of approximately 11 electrons and a gain of 13.6 electrons/ADU (Analog to Digital Unit). The bias level was $\approx$100 ADUs and varied less than 2% over a night. The dark current was measured to be less than the uncertainty in the bias level for the longest exposures used. Although the MASCOT is linear to better than 1%, all frames were typically exposed to the same signal level, including the flat frames. The MIS was used first to find the field and then as a guider so that any telescope tracking errors were insignificant.

I determined that there was no systematic variation of the bias level during a night and that the random variations were less than 2 ADUs. Bias measurements were made at the beginning and end of each night. Flat frames were taken nearly every night using a prepared spot inside the dome, the twilight sky, or both. A set of three to five Titan observations of $\approx$1s exposure were always observed before and after Hyperion to monitor sky conditions over short timescales. Furthermore, Titan was observed throughout the night to obtain an accurate determination of the extinction coefficient. Titan is constant after correction to mean opposition magnitude (see the next section). Landolt (1983) standard stars were observed on approximately one third of the nights and were extensively observed on three nights to accurately determine the color correction and second-order extinction correction (both of which were small, the latter negligible). The Landolt standard stars I observed were 106-700, 106-834, 107-970, HD149382, 109-747, and 110-340. Of these, 107-970 was found to differ from the tabulated value by 0.316 magnitudes: $R_{meas} = 10.082 \pm 0.016$ on June 3, 1987 at 5:07:59 UT and $R_{Landolt} = 9.766 \pm 0.013$. Independent observations by John Kruper (1987) confirmed that 107-970 was not at the magnitude tabulated by Landolt. In his paper, Landolt (1983) notes that 107-970 is variable.

Typically, Hyperion was observed for at least one half the night. No observations were made at greater than 2.5 airmasses and most observations were at less than 2.0 airmasses. Hyperion was located by calculating offsets to the Saturn ephemeris based on the orbital elements found in the Astronomical Almanac. This is more accurate than the tabulated offsets in the Astronomical Almanac. Hyperion's motion in the sky was easily detected over a time period of 15 minutes, confirming it's identity. Although most of the light from Saturn around Hyperion was masked, exposure times ranged from 100 to 600s depending on Hyperion's position in its orbit and its proximity to Saturn which varied from 80" to 240". In addition, the telescope aperture size and the phase and position of the moon affected the exposure time. For consistency, exposures were taken such that the total signal was approximately 90% of the saturated value of the CCD, typically 300s. In order to detect nearby stars and cosmic rays as Hyperion moved through the star field, an average of 11 independent Hyperion observations were made each night. I rejected some of these observations, however, because of background stars or cosmic rays near Hyperion (within about 3"). The actual number of observations used in the final analysis is given in Table V. A large number of independent observations also allowed a check on the consistency of the internal and external uncertainties.

I observed Hyperion for 13 weeks straddling the time of Saturn opposition. The observations were made with minimized scattered light from Saturn. Careful measurements of extinction coefficients and color corrections were made for greater accuracy. Since precise observations are necessary for this project, I have included only observations from MHO because I had consistently clear weather and a good telescope/detector combination. CTIO observations are not included because sky background subtraction was inaccurate when performed with an aperture photometer. Lowell Observatory observations are not included because of marginal weather. Note that the sampling rate is typically better than the observation per 1.5 nights necessary to unambiguously constrain Hyperion's rotation state (see Section II).

Table V. MHO Observations

Date	Day[a]	Phase[b]	r[c]	Δ[d]	N[e]	R Mag[f]
06/01	152.4	0.90	10.028	9.023	2	14.107 ± 0.016
06/03	154.4	0.70	10.028	9.020	6	14.360 ± 0.014
06/08	159.3	0.15	10.028	9.014	3	13.952 ± 0.019
06/09	160.2	0.03	10.028	9.014	9	13.826 ± 0.006
06/10	161.3	0.10	10.028	9.014	7	14.101 ± 0.042
06/11	162.4	0.23	10.028	9.014	6	14.124 ± 0.021
06/13	164.4	0.48	10.028	9.016	6	14.046 ± 0.083
06/14	165.3	0.60	10.029	9.017	9	14.095 ± 0.025
06/15	166.2	0.70	10.029	9.019	8	14.151 ± 0.006
06/16	167.2	0.80	10.029	9.021	12	14.131 ± 0.016
06/17	168.4	0.90	10.029	9.023	7	14.419 ± 0.009
06/18	169.2	1.00	10.029	9.025	11	14.431 ± 0.005
06/19	170.3	1.13	10.029	9.028	10	14.445 ± 0.006
06/21	172.4	1.38	10.029	9.035	7	14.146 ± 0.003
06/22	173.4	1.50	10.029	9.038	7	14.236 ± 0.006
06/23	174.4	1.60	10.029	9.042	9	14.216 ± 0.006
06/24	175.2	1.70	10.029	9.046	3	14.355 ± 0.022
06/29	180.2	2.28	10.030	9.072	5	14.315 ± 0.016
06/30	181.2	2.40	10.030	9.077	6	14.261 ± 0.005
07/02	183.3	2.60	10.030	9.089	7	14.568 ± 0.008
07/03	184.3	2.70	10.030	9.098	9	14.733 ± 0.011
07/04	185.3	2.80	10.030	9.102	6	14.490 ± 0.010
07/05	186.2	2.90	10.030	9.112	17	14.405 ± 0.005
07/06	187.2	3.00	10.030	9.119	7	14.560 ± 0.022
07/07	188.3	3.10	10.030	9.127	11	14.491 ± 0.004
07/08	189.2	3.20	10.030	9.136	16	14.559 ± 0.025
07/09	190.2	3.30	10.030	9.144	9	14.691 ± 0.016
07/11	192.2	3.50	10.030	9.161	20	14.312 ± 0.007
07/12	193.3	3.60	10.030	9.170	6	14.385 ± 0.016
07/13	194.2	3.70	10.030	9.179	11	14.485 ± 0.007
07/14	195.2	3.80	10.031	9.189	13	14.485 ± 0.006
07/17	198.2	4.08	10.031	9.219	7	14.430 ± 0.007
07/19	200.2	4.23	10.031	9.240	7	14.514 ± 0.004
07/21	202.2	4.38	10.031	9.262	15	14.587 ± 0.005
07/22	203.2	4.45	10.031	9.273	3	14.567 ± 0.006
07/23	204.2	4.53	10.031	9.284	11	14.414 ± 0.004
07/24	205.2	4.60	10.031	9.297	8	14.343 ± 0.022
08/04	216.2	5.43	10.032	9.438	6	14.572 ± 0.017

a   Day number after January 0, 1987.
b   Solar phase angle in degrees.
c   Heliocentric distance (AU).
d   Geocentric distance (AU).
e   Total number of independent Hyperion observations.
f   Measured Johnson R magnitude (nightly mean).

IV. DATA REDUCTION

Processing the images to obtain reliable, accurate magnitudes of Hyperion involved the following steps: flattening the raw images, subtracting the background sky gradient, performing photometry of Hyperion in a crowded star field, conversion of instrumental magnitudes to Johnson magnitudes, and correcting for phase and geometry effects.

In general, flattening the frames for an object as bright as Hyperion would not be very critical because the pixel to pixel variation is less than a few percent. However, there is a faint ($\leq$ 1%) grid pattern on all of the frames, which makes background fitting susceptible to systematic error. Therefore, all bias-subtracted frames were divided by normalized bias-subtracted flat fields. This eliminated the grid pattern and the frames were flattened to better than 0.1 percent. On the nights in which I had both dome flats and twilight flats, the final magnitudes of dome flattened and twilight flattened images differed by less than 0.003 magnitudes.

From the discussion of sky subtraction with an aperture photometer, it is apparent that sky gradient subtraction is necessary for accurate photometry of the Hyperion images. Sky subtraction was done using IRAF (Image Reduction and Analysis Facility) (Tody 1986) tasks. Typically, I would use a 2-dimensional Chebyshev 6th-order polynomial to fit for the background gradient. The best parameters for the fit were determined experimentally by trying different order polynomials and other parameters until the fits gave the smallest residuals. On nights when Hyperion was near elongation or conjunction, such that it was aligned along the telescope spider diffraction spikes, I would use a similar one-dimensional fit for each row or column. All subtractions were good, even when Hyperion was near other bright stars. This is illustrated in Figure 5, a grey scale image (a) before and (b) after the sky gradient subtraction. Figure 6 is a surface plot of the same image. This is a representative case of background gradient subtraction. Background subtraction was performed on every Hyperion image with similar good results.

Photometry of Hyperion was further complicated because it was near the Milky Way (galactic longitude $\approx 1°$, latitude $\approx 12°$). There were usually 10 or more stars nearby, each bright enough to cause greater than 1% difference in the final value of Hyperion's magnitude. It is possible to accurately subtract the nearby stars and perform the usual aperture photometry using DAOPHOT (Stetson 1987), a crowded-field photometry program. This program was designed to use some of the stars in the frame as a model for the point-spread function (psf) that can then be fitted and subtracted. For each Hyperion frame, I identified every star near Hyperion, within ≈ 20 pixels (12"). Then, choosing the brightest stars in the frame, I obtained a model psf which was scaled and subtracted from all the identified stars.
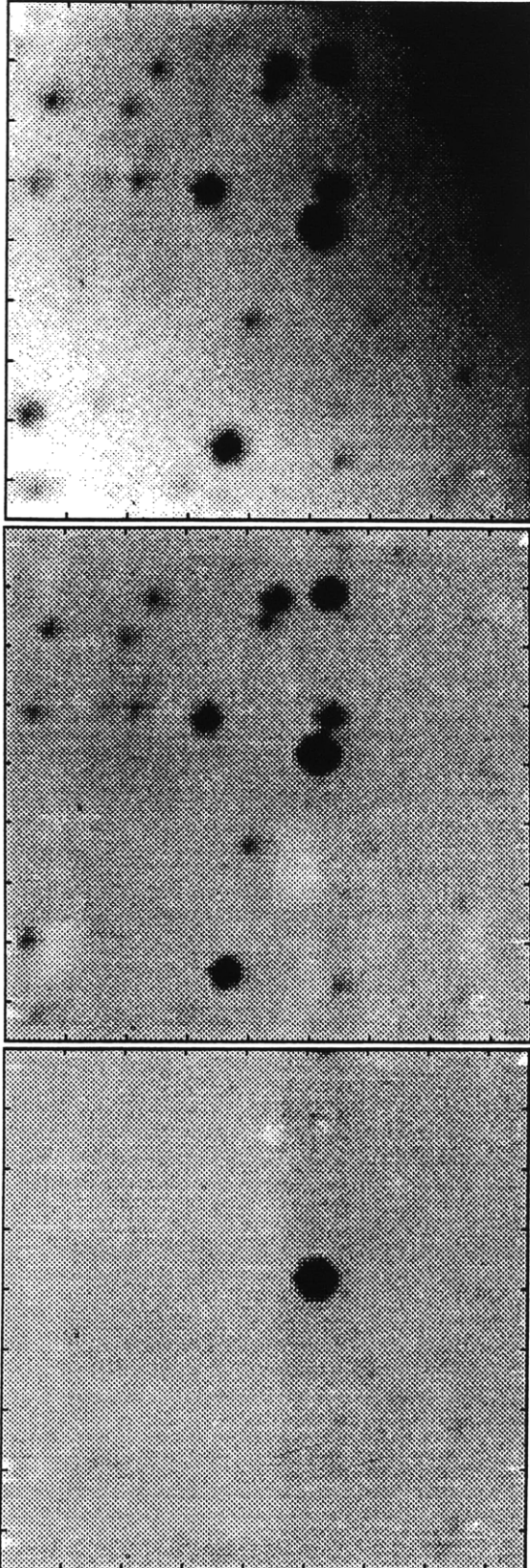
Figure 5. Grey -scale images illustrating the reduction of the flattened Hyperion frames. (a) is the flattened Hyperion image. Notice the strong background gradient. (b) is the same image after fitting the sky gradient and subtraction from (a). (c) is after point-spread-function fitting and subtraction of the surrounding stars. The residual sky variation is less than 1 percent in the region near Hyperion. Hyperion is the largest source in all images. These are representative of the images I obtained and reduced.
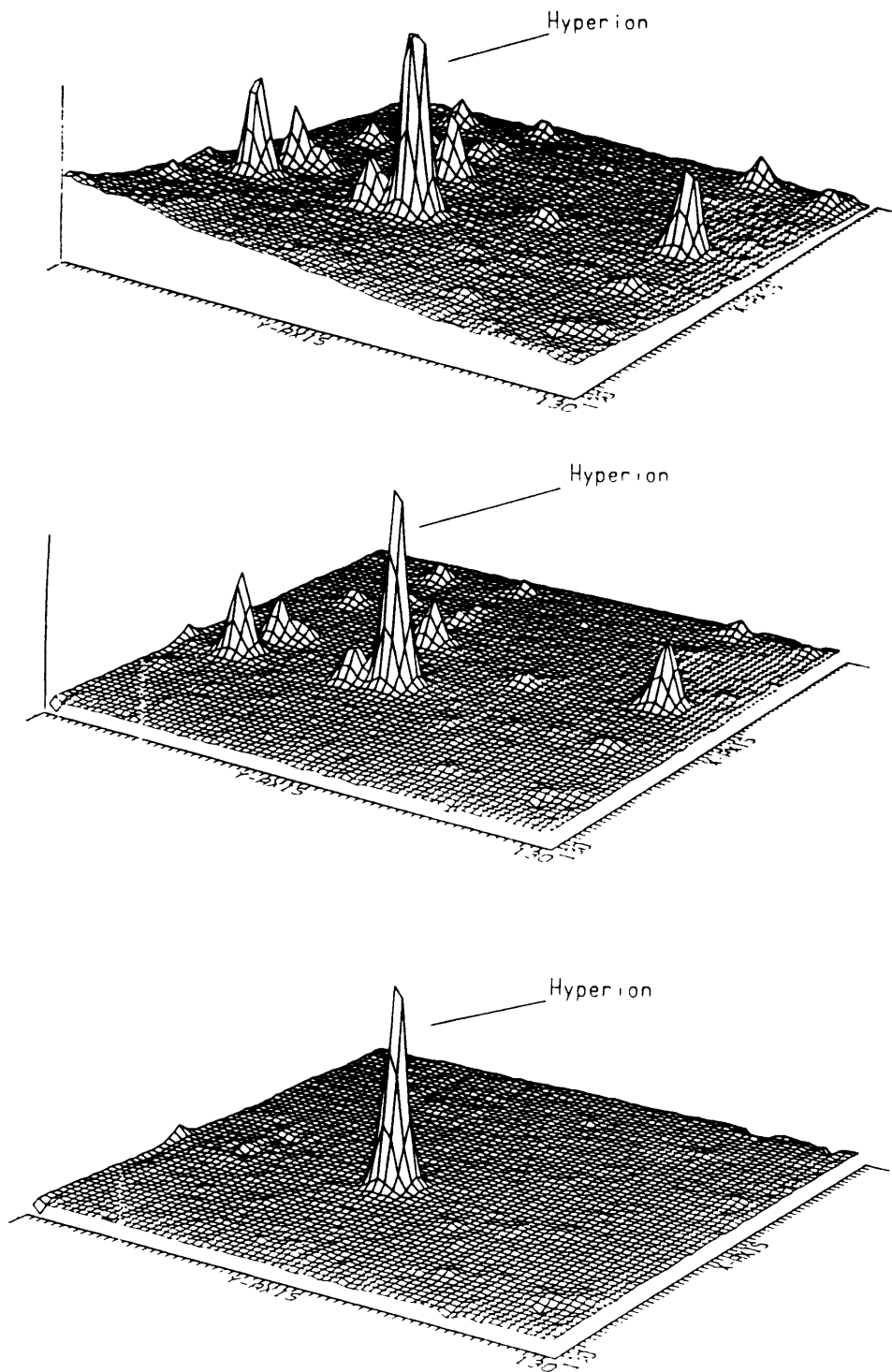
Figure 6.   Surface plots illustrating the reduction of the flattened Hyperion frames. As in Figure 5, (a) is
the flattened Hyperion image. (b) is the same image after fitting the sky gradient and
subtraction from (a). (c) is after point-spread-function fitting and subtraction of the
surrounding stars. The residual sky variation is less than 1 percent in the region near
Hyperion. These are representative of the images I obtained and reduced.

At this point, normal aperture photometry could be performed, and I chose an aperture size that included greater than 99% of the light, as determined by radial intensity profiles, typically 15 pixels (9") radius. Figure 5(c) shows the grey-scale image and Figure 6(c) the surface plot of the Hyperion frame after subtracting the nearby stars with DAOPHOT. Note that even the very bright star nearby subtracted well. This figure is an example of star subtraction that is again representative of the fields encountered. This same method was used with Titan and standard star observations to avoid any systematic error, except that no sky subtraction or psf fitting was necessary, even when Titan was at conjunction. I used DAOPHOT to do photometry of stars as faint as Hyperion in the same background sky gradient with very good results. All of these star observations were within ≈ 0.01 magnitudes after correction for extinction.

The photometry was converted to magnitudes using

$$R = -2.5 \log C - kX + \varepsilon(V - R) + \zeta$$

where R is the Johnson R magnitude (similarly for V),
C is the number of counts (ADUs) per second,
k is the extinction coefficient,
X is the airmass,
ε is the transformation (color) coefficient, and
ζ is the zero point (Hendon and Kaitchuck 1982).

The extinction and zero point were measured each night. All nights were photometric to at least 4%, and most to 1-2%, as determined from inspection of the extinction curves and calculation of the formal uncertainties. The color transformation was measured three times and was found to be virtually the same for both the 1.3m and 2.4m telescopes, which is to be expected because the filters and detector were the same. Second-order extinction coefficients were also calculated but were found to be negligible. The R color transformation coefficient was calculated to be ε_R = -0.066 ± 0.009. Since this is a small coefficient, even a relatively large uncertainty in the color of Hyperion would cause a minor error in the final magnitude. ε_V is even smaller: ε_V = -0.001 ± 0.012. The color of Hyperion was measured on 6 separate nights and was found to be V-R = 0.41 ± 0.02 and constant within the uncertainty. Table VI is a tabulation of these measurements. Landolt standards were used for comparison on these nights, and Titan was used as a standard on other nights.

Table VI. Hyperion V-R Color

Date, 1987	V	V-R
06/08	14.01 ± 0.02	0.38 ± 0.02
06/09	14.57 ± 0.04	0.46 ± 0.05
06/17	14.60 ± 0.02	0.40 ± 0.02
07/03	14.60 ± 0.03	0.45 ± 0.04
07/05	14.62 ± 0.03	0.40 ± 0.05
07/18	14.54 ± 0.04	0.43 ± 0.06

I chose to use Titan as a standard because its proximity to Hyperion allowed me to check the sky variation efficiently while the extinction correction was essentially the same as Hyperion. Titan has been shown to be stable over timescales of months (Andersson 1977). I found no secular change in Titan's magnitude on the 9 nights measured over a 2 month period. The rms variation of these Titan magnitudes, after reduction to mean opposition magnitude, is 0.005 magnitudes. Any systematic error due to using Titan as a standard is insignificant. I used a phase coefficient of β_R = 0.0015 ± 0.0010 magnitudes/degree based on extrapolation of measurements by Andersson (1974) and comparison of Noland *et al.* (1974) uvbyr data; β_V = 0.0036 ± 0.0012 (Andersson 1974). For Titan, I found R = 7.66 ± 0.01 and V = 8.23 ± 0.04.

I reduced all Hyperion, Titan, and standard star photometry to R magnitudes, as defined above. Of the average 9 independent observations of Hyperion per night (see Table V), I calculated a formal propagated uncertainty as well as the rms uncertainty. Typically, these internal and external uncertainties agreed, but when they did not, I chose the larger uncertainty and these are the values listed in Table V. Although some of the uncertainties in my reduced magnitudes are small, <0.01 magnitudes, they are realistic because the large number of observations provided a check on the results. On no night did I find an unambiguous trend in the brightness variation of Hyperion. Hyperion's brightness was constant over a time period of 6 hours at the 0.01 magnitude level. Table V lists the raw mean nightly magnitudes of the MHO Hyperion observations. Figure 7 is a plot of the data listed in Table V, the raw lightcurve.
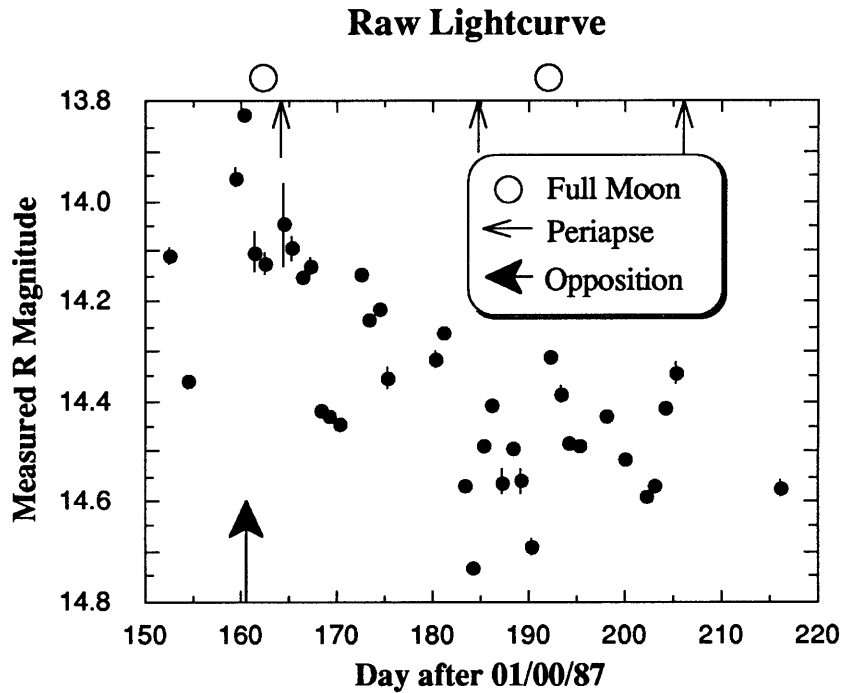
Raw Lightcurve

Figure 7.   Raw Hyperion lightcurve. Measured Johnson R magnitudes uncorrected for mean opposition distance or solar phase angle versus time in days after 01/00/87 (see Table V). Error bars are not shown for points having a uncertainty less than 0.01 magnitude (the size of the dot).

Figure 8 is a plot of the measured magnitudes versus solar phase angle. There is an obvious brightening with decreasing phase angle and a surge of 0.2 to 0.4 magnitudes at phase angles less than $\approx 0.3°$. The exact size of the opposition surge is difficult to determine because of the rotational variation. This variation due to rotation will necessarily make any phase correction inaccurate. Fortunately, the analysis is relatively insensitive to phase correction, as will be shown later. With this in mind, I use the H, G phase model (Bowell, Harris, and Lumme 1987) developed for asteroids and satellites. I first make the geometric correction to mean opposition distance using the relation

$$R'(\alpha) = R - 5\log\frac{r\Delta}{r_s\Delta_s}$$

where $R'(\alpha)$ = the mean opposition R magnitude uncorrected for solar phase,

r = heliocentric distance,

Δ = geocentric distance,

r_s = 9.54 AU, Saturn's mean heliocentric distance, and

Δ_s = 8.54 AU, Saturn's mean geocentric distance.

The H, G model is an empirical model written in the form:

$$R'(\alpha) = H - 2.5 \log \left[(1 - G)\Phi_1(\alpha) + G\Phi_2(\alpha) \right]$$

where H = magnitude at mean brightness corrected to mean opposition distance and zero solar phase angle, G = slope parameter, and $\Phi_i \equiv \exp [-A_i (\tan \alpha/2)^{B_i}]$, with the parameters (from Bowell, Harris, and Lumme 1987):

$A_1 = 3.331$ $B_1 = 0.628$, and
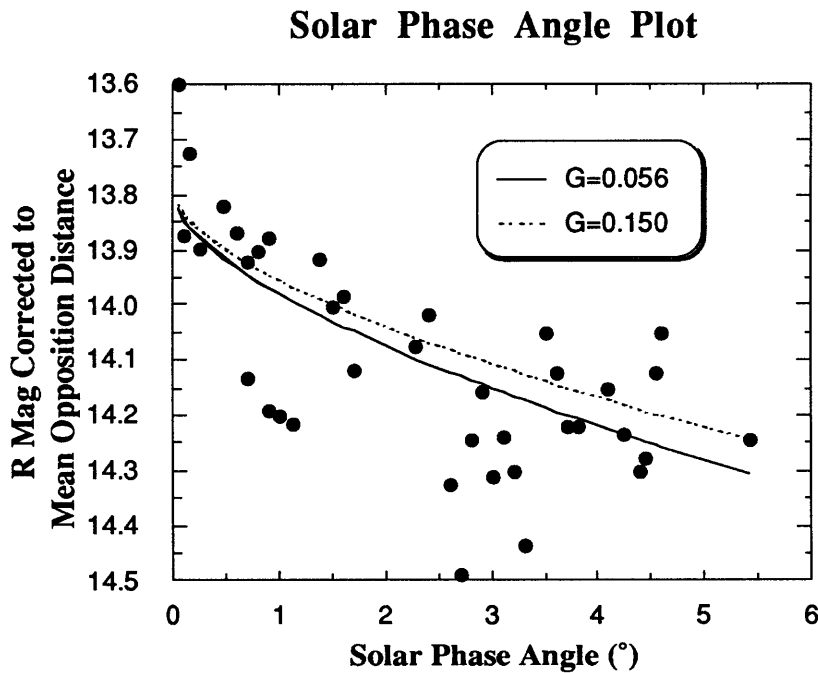$A_2 = 1.866$ $B_2 = 1.217$.

Solar Phase Angle Plot

Figure 8.   Hyperion R magnitudes corrected to mean opposition distance (r_s=9.54 A.U. and Δ_s=8.54 A.U.) versus solar phase angle in degrees (see Table V). The solid line is the least-squares fit to the H, G phase model: H=13.81, G=0.56. The dotted line is a mean value for C-type asteroids, which have albedos similar to Hyperion's. Error bars are not shown for points having a uncertainty less than 0.01 mag.

The H, G phase model fit is shown in Figure 8, using the fitted values H = 13.81 ± 0.05, and G = 0.056 ± 0.14 for the solid line. For comparison, asteroid 1 Ceres has a slope parameter of G = 0.083. Hyperion's albedo is most similar to C-type asteroids, which have a mean slope parameter of G = 0.15 (Bowell *et al.* 1987). This value of G is also plotted, as a dotted line, in Figure 8. Given the scatter in the data, it is impossible to tell which is the "true" value. It is important to note 1) Hyperion has a rotational brightness

variation of about 50%, making the fit inexact, 2) the H, G model may not be adequate for objects that exhibit a large opposition surge (as stated by Bowell *et al.* 1987), and 3) the exact form of the phase correction does not affect the period-fitting analysis. The zero-phase lightcurve is shown in Figure 9. In this figure, the mean opposition magnitudes of the Hyperion nightly means corrected to zero solar phase angle using the H, G least-squares fitted values are plotted versus the time of observation. In the next section, I discuss how the period fitting is insensitive to the exact form of the phase-corrected lightcurve.
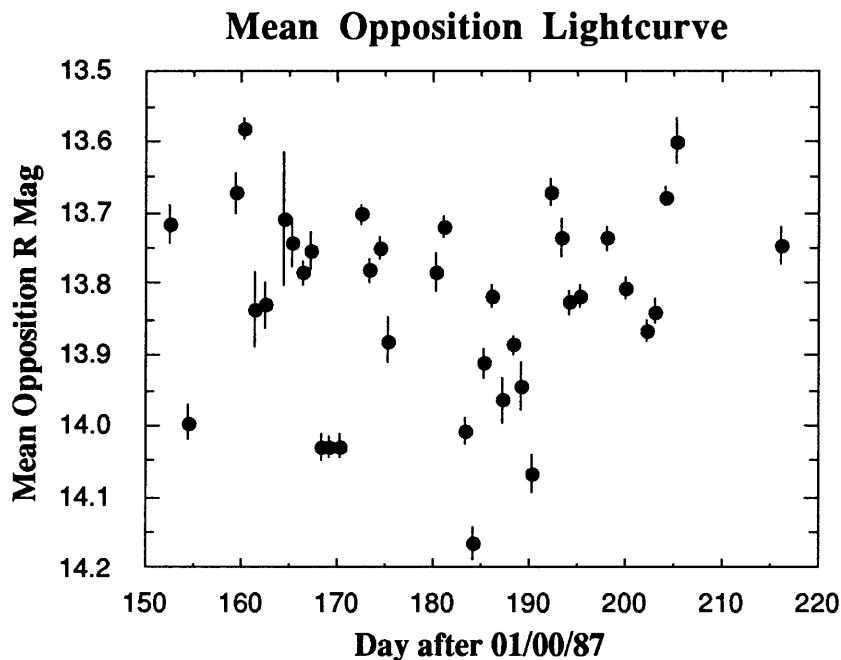
Mean Opposition Lightcurve

Figure 9.   Hyperion lightcurve corrected to zero solar phase angle (α=0) and mean opposition distance (r_s=9.54 A.U. and Δ_s=8.54 A.U.). Note the change in scale from the previous two figures.

There were four major steps to reducing my data to standard magnitudes. Flattening and geometry/phase corrections are standard and well-established procedures. In my case, the phase correction was made difficult due to the unknown aspect of Hyperion, although this can be corrected with simultaneous fitting to the chaotic dynamics (see the next section). One of the aspects of precise photometry of Hyperion is its position in the background light gradient due to its proximity to Saturn. Without background gradient subtraction, photometry is plagued by large random errors as exemplified by direct experimentation with my images and the use of an aperture photometer. Photometry was further complicated by the large number of background stars nearby. Computing a psf using field stars, it was possible to subtract these stars and perform normal aperture photometry. These procedures were shown to be valid by reproducing standard star and

Titan magnitudes, as well as faint field stars as they apparently move through Saturn's scattered light field. Furthermore, an average of 9 independent Hyperion observations were made each photometric night and it was shown that there was no measurable variation during a six hour period.

V. ANALYSIS

Analysis of my observations will be carried out on two independent levels: period determination and dynamical fitting. First, I will analyze the data for any coherent rotation period at timescales ranging from hours to months. It will be demonstrated that there is no plausible period that can describe the lightcurve, even considering the observational and phase-fitting uncertainties (Klavetter 1989). Because of this lack of a coherent period in the lightcurve and the theoretical expectation that Hyperion is chaotically tumbling, a second analysis will be carried out based on the dynamical model derived in Section II. It is important to note that any conclusion inferred from the period determination is independent of the dynamical fitting.

In subsection A, I will discuss the period determination techniques used to examine any regularities in Hyperion's lightcurve. In the next subsection, I will derive various modifications to the model presented in Section II such that chaotic rotation can be modeled and fit to my lightcurve. In doing so, four parameters in addition to the state variables will be determined from the analysis: the mean opposition magnitude, the phase coefficient or slope parameter, and the two principal moments of inertia normalized to the third. In subsection C, a general method of determining the initial condition of a lightcurve is presented. In subsection D, I will present results of fits to the MHO lightcurve based on a small fraction of phase space searched.

A. PERIOD DETERMINATION

The Hyperion lightcurve was analyzed with a Phase-Dispersion Minimization (pdm) algorithm. This technique yields an unbiased best period with no dependence on a fitting function (Stellingwerf 1978). With pdm analysis a range of periods are assumed, and the lightcurve is folded back upon itself. For each period in the range, the data are then sorted in a manner such that there are at least a few data points in each bin. The dispersion about the mean value is calculated for each bin and the total dispersion is calculated for the periods tested. This allows the best period for any given data set to be determined by finding the minimum in the plot of period versus dispersion. When the dispersion is small, the brightness at any given phase is approximately the same and the data is well described by that period. Pdm analysis does not use a fitting function, so there is no prior assumption about the type of periodicity that is detected by inspection of the pdm plot.
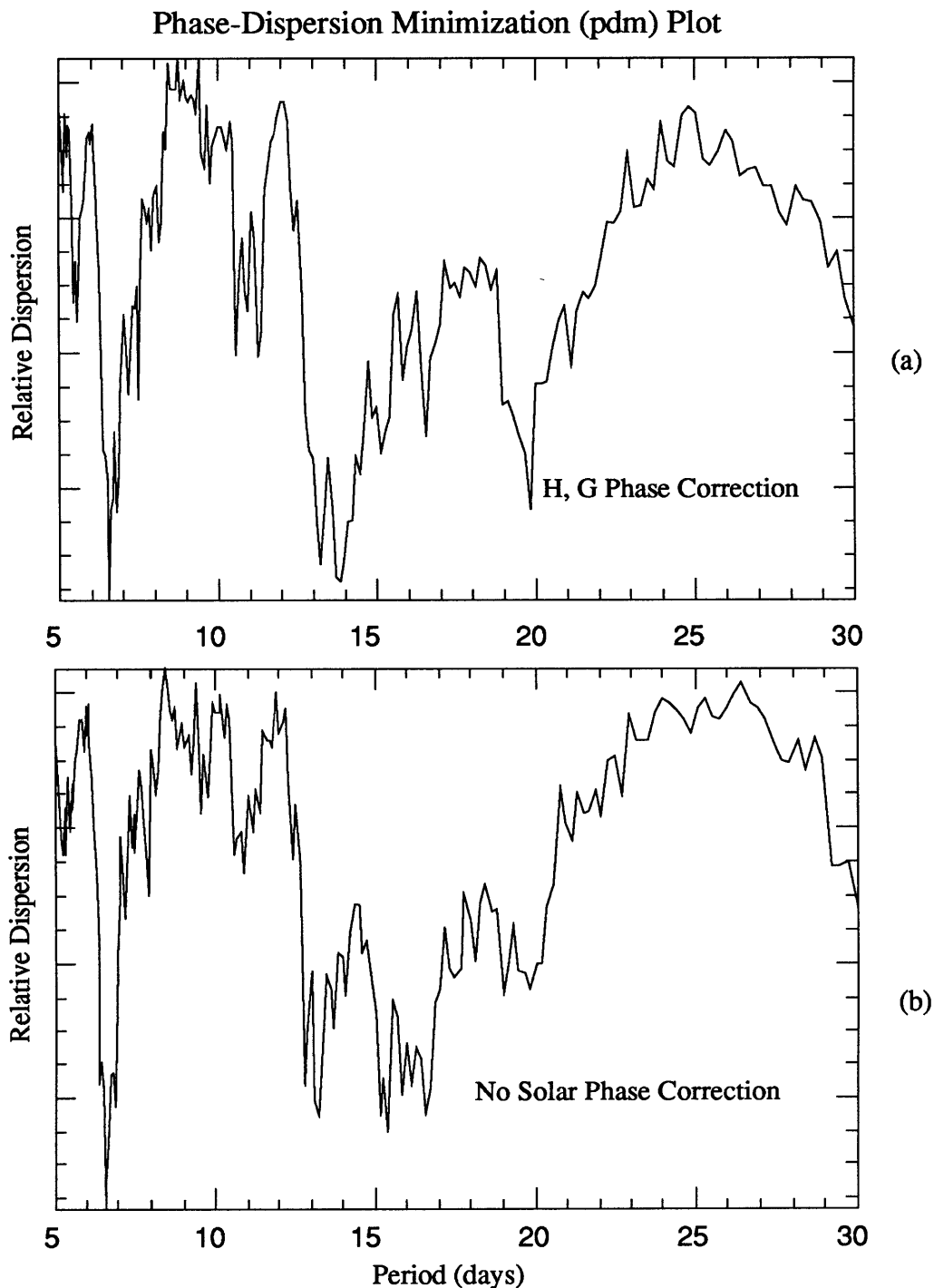
Phase-Dispersion Minimization (pdm) Plot

Figure 10. Phase Dispersion Minimization (pdm) plot of the MHO lightcurve with (a) H, G phase correction (Figure 9) and (b) no correction for solar phase angle (Figure 7). The best period is at 6.6 days. The similarity of the two plots indicates that the period analysis is insensitive to the phase correction. The ordinate is a relative measure of the dispersion normalized to the best period. The dispersion expected from the observational uncertainty is a factor of 10 less than what is plotted. The statistical significance of the best period is shown to be small (see Figure 11).

The pdm plots of the MHO lightcurve agree to within a few percent for three methods of phase correction: 1) the H and G phase correction (Bowell *et al.* 1987), 2) linear phase correction with some or all of the observations, and 3) no phase correction. With pdm analysis, the best period found for the mean opposition magnitude lightcurve of the nightly means (Figure 9) is 6.6 days. This is shown in the pdm plot in Figure 10(a). The statistical significance of this period can be measured by comparing the uncertainties of the data with the variances of each bin. For any given period, the mean over all bins of the square root of the variance should be comparable to the uncertainties in the data for an acceptable fit. This quantity for the 6.6 day period is 0.11 magnitudes, a factor of 5 to 10 larger than a typical observational uncertainty of 0.01–0.02 magnitudes. Another measure of the significance of the fit is demonstrated by inspection of the phase plot in Figure 11 in which the data are folded back using the 6.6 day period. Note the large differences at various phases, indicating the fit is not good. The phase plot of 13.8 days was also unconvincing as a period. Neither the 6.6 day nor the 13.8 day period is a simple fraction of the orbital period of 21.3 days or some integer multiple of the sampling rate.
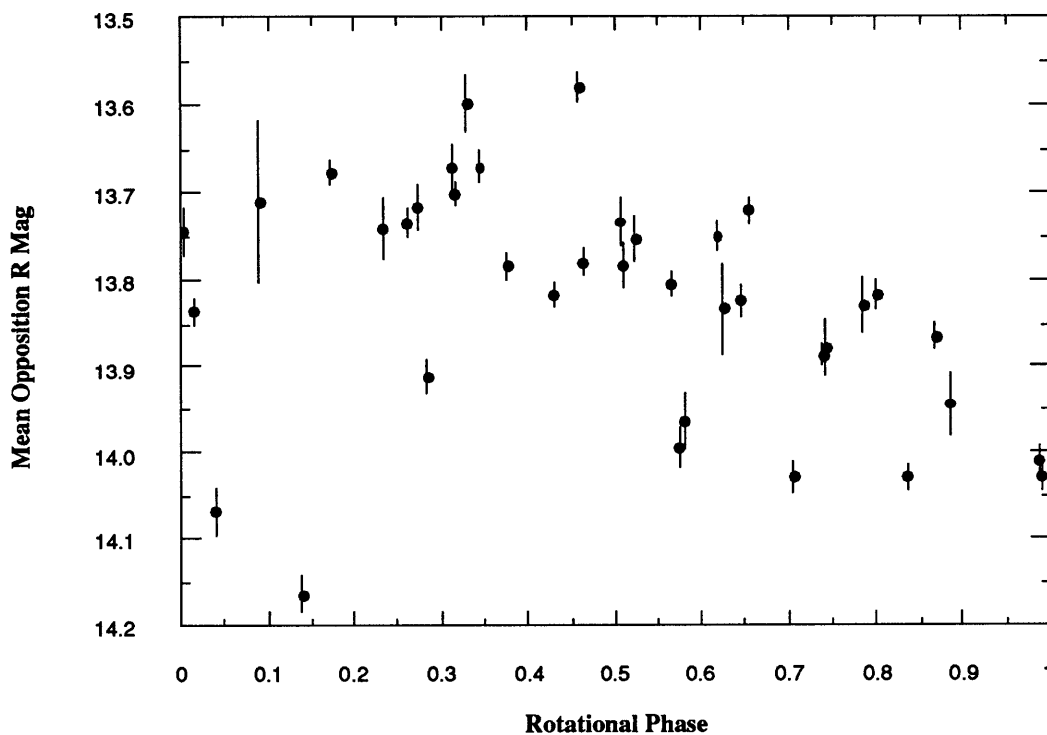
Rotational Phase Plot

Figure 11.   A rotational phase plot. The MHO lightcurve folded back using the best-fit period of pdm analysis, 6.6 days (see Figure 10). The large variations at various phases indicate that this is not a good fit.

The period for the best fit is similar to those periods derived from numerical simulations of a chaotically rotating Hyperion-modeled ellipsoid using traditional least-squares analysis (Peale 1986, Wisdom and Peale 1984). Indeed, Peale and Wisdom (1984) found that it was easy to define intervals of numerically generated lightcurves that yielded desired periods. Although pdm analysis may be used to determine the best period over a given time interval, this period may not have physical meaning for the system under consideration. The statistical comparison above and the rotational phase plot shown in Figure 11 demonstrate that the best period chosen through pdm analysis, is not a good fit.

Similarly, a best period was calculated using the entire data set instead of the nightly means. The pdm plot for the entire data set is shown in Figure 12. All periods from 2 hours to 5 days were tested with the entire data set. There is an obvious aliasing problem since the best fit periods are multiples of one day, the average sampling rate. The dispersion, however, is again a factor of 10 larger than that expected from the observational uncertainty, indicating that none of these fits are adequate to describe the lightcurve. Rotational phase plots of the best periods from the pdm plot confirm that none of the best periods are good fits. This demonstrates that short, or asteroidal, periods are not fit by the data, consistent with the observational result that no measurable trends were seen in any of the nightly variations.

Phase-Dispersion Minimization Plot
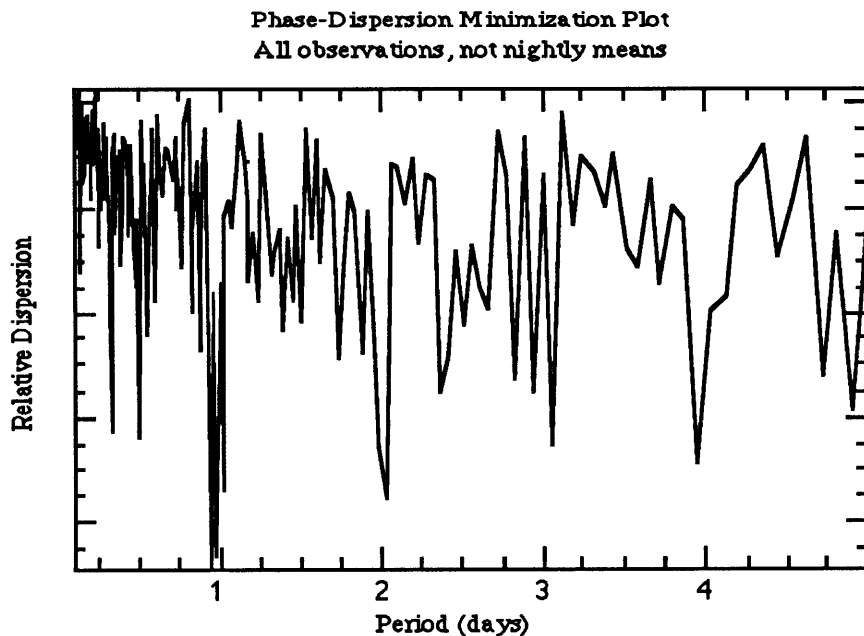**All observations, not nightly means**

Figure 12.   Phase Dispersion Minimization (pdm) plot of the entire data set, not the nightly means. The best periods are multiples of the sampling rate of one day. The ordinate is a relative measure of the normalized dispersion. The dispersion expected from the observational uncertainty is 10 times less than what is plotted, indicating that none of the best fits adequately describes the entire data set.

Various phase functions for both the nightly means and the entire data set were analyzed using the pdm technique. All phase plots for absolute and local minima and corresponding harmonics were plotted and found to be as scattered as the rotational phase plot of Figure 11. For comparison, the pdm plot for the nightly means with no phase correction is shown in Figure 10(b), corresponding to the raw lightcurve of Figure 7. The absolute minimum value of the pdm plot shown in Figure 10(b) agrees with that value found using the H, G model phase correction, shown in Figure 10(a), and the overall structure is similar. No well-defined period was found for any of the minima. No period from 1 hour to 50 days fits the data set satisfactorily.

B. MODIFICATIONS TO THE DYNAMICAL MODEL

The results of pdm analysis show that there is no well-defined periodic variation in the lightcurve obtained from observations taken at MHO. This is consistent with a chaotic rotation state as predicted by Wisdom *et al.* (1984). Since the uncertainties are small and the sampling is on the order of one observation per day, it is not reasonable to conclude that Hyperion is in a regular, undetected, rotation state. There will be further discussion of this in the next section. Now I will attempt to fit the model based on the dynamics as developed in Section II to the lightcurve produced in Section IV. Some modifications need to be made, however, to convert the rotation state as defined by the equations of motion to the lightcurve as seen from Earth.

The data were first corrected for light travel time. What is observed on Earth is the position 70 or more minutes prior to the time of the observation at the distance of Hyperion. To determine these light travel times for each observation, I interpolated the values given in the 1987 *Astronomical Almanac*. Although Hyperion's brightness does not change significantly on such timescales, chaotic motion is extremely sensitive to the initial condition. A difference of 70 minutes in the time of observation at the beginning of the lightcurve can propagate to a hundredth of a magnitude or more difference at the end of my lightcurve. This is of the same order as a typical uncertainty in my lightcurve.

In order to compare my lightcurve with the model, the position of Hyperion in its orbit must be determined. I used the general formulae from the *Explanatory Supplement to the Astronomical Ephemeris and the American Ephemeris and Nautical Almanac* to calculate the mean anomaly, the eccentricity, and the other orbital elements. Solving Kepler's equation gives the eccentric anomaly which can, in turn, be transformed to the true anomaly. The true anomaly is the state variable needed. The details of the procedure are given in Appendix E.

The dynamical model, as it has been developed in Section II, allows the rotation state to be calculated given an initial rotation state. In the case of Hyperion, the rotation state consists of the three angles necessary to specify its orientation in space, the three angular velocities defined in equation (2), the three principal moments of inertia, and a time variable such as the true anomaly. In general, the principal moments of inertia for a homogeneous ellipsoid is given by the equation

$$A = \left(\frac{b^2 + c^2}{5} \right) m$$

where A is one of the principal moments of inertia, b and c are the semi-axes, and m is the mass. The equation is cyclic for B and C. Because there is no adequate mass determination of Hyperion, the moments cannot be computed. Following the procedure outlined by Wisdom *et al.* (1984), I normalized the principal moments by the largest, C. Thus, whenever referring to the principal moments of inertia, it will imply the ratios A/C, B/C, and the redundant C/C. Note that the equations of motion are still completely general and independent of the actual value of C because the Euler Equations are linear in the moments. Although the absolute values of the moments are not known, the dynamics can be computed using this formalism.

Determination of the rotation state does not allow direct comparison with the lightcurve. Integration of the lightcurve produces a set of dynamical state variables which must be compared to the lightcurve, which is a set of magnitudes at certain times. The relative magnitude of a uniform ellipsoid depends upon the orientation of the ellipsoid relative to Earth and its position in its orbit, independent of the velocity state variables. The equation of an ellipsoid is

$$1 = \frac{x'^2}{a^2} + \frac{y'^2}{b^2} + \frac{z'^2}{c^2}$$

where the primed coordinates represent the body frame and $a > b > c$ are the principal semi-axes. A set of three rotations can be applied to the body axes to find the equation of the Hyperion ellipsoid in the Saturnocentric coordinate system. These are the Euler (Wisdom) rotations defined in Section II. The matrix that converts the body coordinates to the Saturnocentric coordinates, $\mathbf{A}$, is calculated in Appendix A. $\vec{x} = \mathbf{A}\vec{x}'$ is used to calculate the equation of the ellipsoid in the unprimed, Saturnocentric, coordinate system.

The projected area of the ellipse is found by substituting the equations for the body axes into the equation of the ellipsoid and differentiating with respect to x to give the projection on the y-z plane. The equations are derived in Appendix F such that the projected area of the ellipsoid can be expressed in the dynamical state variables.

The projected area of the Hyperion ellipsoid is now known in the Saturnocentric coordinate system. Because the observations were made from Earth, however, a transformation of the Saturnocentric coordinate system to a geocentric coordinate system must be made. The $\vec{e}$ coordinate system is an Earth-based system defined as follows: the e_1 axis is parallel to the Earth-to-Saturn (or Hyperion) vector, the e_3 axis is perpendicular to the plane of the ecliptic, and the e_2 axis completes a right-handed coordinate system. The transformation to the geocentric axes involves two rotations. The first rotation, as shown in Figure 13(a), is by an angle, ξ, about the z axis. This rotation aligns the x axis with the e_1 axis. The angle ξ is the projection of $\hat{x} \cdot \hat{e}_1$ onto the ecliptic. ξ is essentially constant over the time Hyperion was observed. It changed by less than 0.7° during this time, so there is negligible error introduced in the projected area by assuming ξ is constant.

The second rotation necessary to transform the Saturnocentric coordinate system to a geocentric one is an angle B about the new y axis to orient Hyperion's orbital plane to the plane of the ecliptic, as shown in Figure 13(b). I used the values of B as tabulated in the *Astronomical Almanac*, interpolated to the appropriate time. The inclination of Hyperion to the plane of the rings, which is the reference plane for the tabulation of B, is 0.4°. The effect of Hyperion's inclination to the calculation of the projected area is negligible and has been ignored.

The rotations, ξ and B, are analogous to a right ascension and declination of Hyperion as viewed from Earth. They differ slightly from right ascension and declination in that ξ has a different zero point than right ascension and B corrects for the inclination of Saturn to the ecliptic . These two rotations, in addition to the above transformation from body axes to Saturnocentric axes, are adequate to transform the rotation state to a projected area as seen from Earth. Appendix F gives the full details of the procedure used to calculate the projected area of Hyperion as seen from Earth from the dynamical state variables.

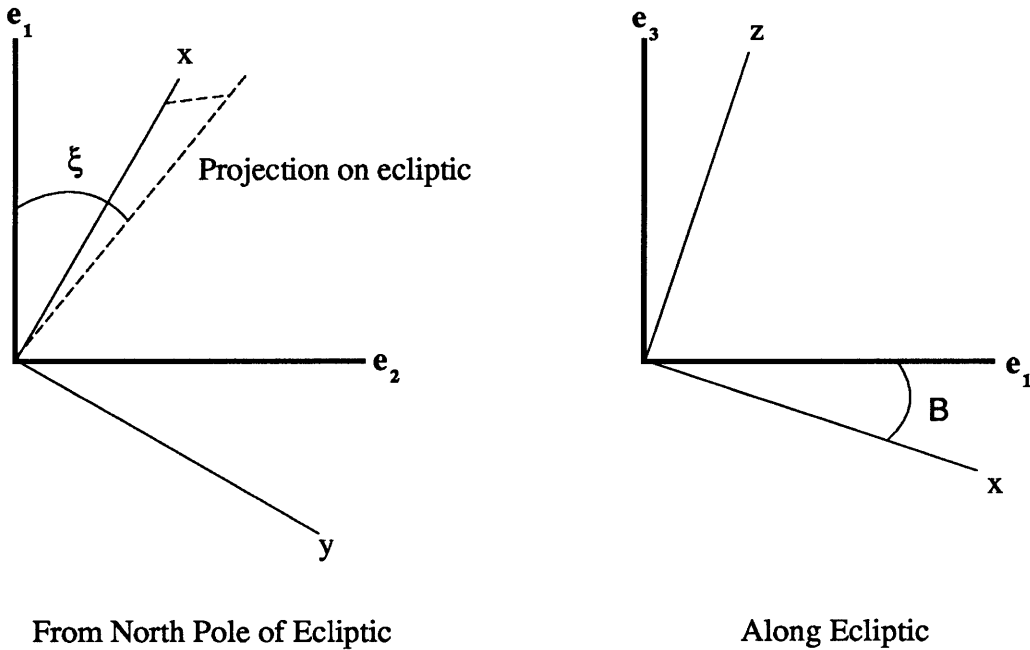From North Pole of Ecliptic   Along Ecliptic

Figure 13.   The two rotations necessary to bring the Saturnocentric frame in line with the geocentric
frame. These are necessary to find the projected area of Hyperion as seen from Earth. The
first rotation is about the Saturnocentric z axis by an angle ξ. This is a projection of the
angle between the Earth-Saturn line and the line of Hyperion's periapse, analogous to a right
ascension of Hyperion as seen from Earth. The second rotation is about the new y axis by an
angle B, analogous to the declination of Hyperion as seen from Earth.

In order to relate the rotation state of Hyperion to my lightcurve, the projected area
must be converted to a magnitude. Assuming albedo remains constant for any aspect of the
satellite, the relative magnitude is $m = -2.5 \log A$, where A is the projected area
normalized to the maximum projected area. There is a constant offset between this
magnitude and the magnitudes obtained from my lightcurve. This number is related to the
mean opposition magnitude and will be one of the parameters used in the fitting process.

The Duxbury values of the principal semi-axes, as reported by Wisdom *et al.* (1984)
were used to compute the projected area of the Hyperion modeled ellipsoid. The best-fit
ellipsoid found has principal semi-axes of 190 x 145 x 114 ± 15 km. This is consistent
with the values given by Thomas and Veverka (1985). The differences in the two
determinations of size are less than 3% in each dimension, much less than the formal
uncertainties. An inspection of Figure 1, one of the highest-resolution *Voyager* images,
shows that Hyperion can have a projection well fit by an ellipse, consistent with
Hyperion's shape being closely approximated by an ellipsoid. The effect of uncertainties in
Hyperion's shape and albedo will be discussed in the next section.

Integration of the equations of motion, given in Appendix D, for the ellipsoid model were performed using the Bulirsch-Stoer method of numerical integration (see Press *et al.* 1986). During the course of an integration, it was not uncommon for the solution to be near a singularity, necessitating a switch to the other coordinate system. The mathematical details of the coordinate conversions are derived in Appendix G.

C. NUMERICAL SIMULATIONS

The model presented is of an ellipsoid in the spin-orbit coupling system of Saturn and Hyperion. An initial condition integrated over time gives the rotation state, and therefore relative magnitude of the system, at any other time, within the precision of the computer. The difficulty is finding the initial condition corresponding to my lightcurve. Numerical simulations indicate that phase space becomes more complex as longer intervals of observations are examined. Figure 14 illustrates this increase in complexity. This plot was obtained by numerically calculating a lightcurve with the same sampling intervals as my MHO lightcurve using a random initial condition chosen to mimic the features seen in that data. I then calculated the sum of the squared residuals, χ^2, normalized to the number of observations for a range of values along the principal axes for both the entire lightcurve and a section of well-sampled points, keeping the other dynamical variables constant at their correct values. The two curves shown in Figure 14 are calculated for the velocity variable along one of the principal axes. Note that the solid line curve associated with the entire lightcurve displays more peaks and valleys than the dashed line corresponding to the lightcurve section. The curve for the entire lightcurve is also much narrower near the value of the known initial condition than the section, although both exhibit approximately the same value at zero displacement from the known initial condition. Thus, a fitting routine would have difficulty finding the absolute minima for the entire lightcurve because of the presence of so many local minima. The same fitting routine would not encounter this difficulty for the curve corresponding to the section.

These results are very general. The same features seen in Figure 14 appear for other initial conditions. Similar curves are calculated for the other velocity components, although the effect is less extreme for the other state variables (see below). The section chosen corresponds to 12 points out of a 13 day sampling interval from the MHO data. The behavior is similar for other well-sampled sections. A gaussian error distribution of 0.03 magnitudes per observation was added to this numerically-generated lightcurve to better simulate a realistic χ^2 distribution.
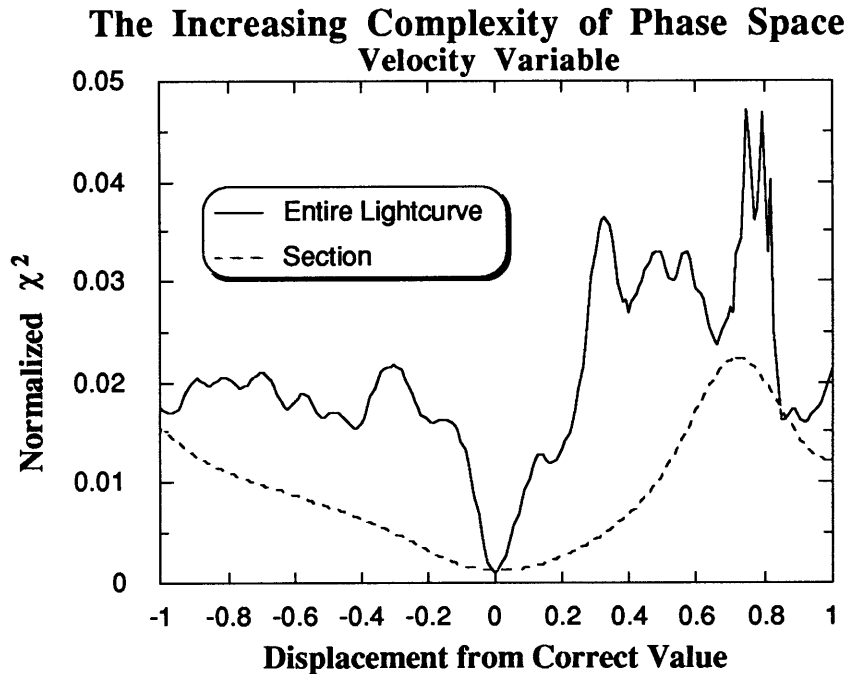
The Increasing Complexity of Phase Space

Figure 14.   An illustration of how the complexity of phase space increases with the number of observations. All dynamical variables were set equal to their known values except for one component of the velocity which varied between plus and minus one rotation/revolution from its correct value. This is plotted along the abscissa. Plotted along the ordinate is the χ^2 per number of points for two data sets. The solid line corresponds to a numerically generated lightcurve at the same sampling rate as the MHO lightcurve (Figure 9), the dashed line to a well-sampled section of that lightcurve, 12 observations in a 13 day interval.

All but one dynamical state variable was kept constant as that one was varied. This is essentially a one-dimensional version of the problem since none of the variables would be known in advance, in general. However, this behavior was seen for the other velocity variables and for different initial conditions. Therefore, a generalized fitting routine would have more success fitting fewer well-sampled observations than fitting the entire lightcurve, although this is somewhat counterintuitive.

A general procedure for determining initial conditions for a Hyperion lightcurve can be outlined. The strategy is to choose a well-sampled portion of the lightcurve as the data set and search all of phase space using the ellipsoid model developed above. The sampling rate, or grid spacing, is discussed below. Once an approximate rotation state is found that matches the data set, the rest of the observations are added singly and fitted to converge on the initial condition. Numerical simulations (Klavetter 1985, unpublished) demonstrate that when using this technique, there is an exponential decrease in the uncertainty of the initial

condition as the number of observations increase. This can be seen in Figure 15, in which the log of the residuals of the moment variables are plotted versus observation number for a lightcurve with known moment ratios. For this plot, data with 0.03 magnitude simulated observational error was fit using the above algorithm and the residuals at each step were plotted. There is a dramatic decrease in the residuals, almost down to machine precision in the 60 day interval (see Klavetter 1985). Wisdom (1987) and Chakrabarty (1988, unpublished) found a similar exponential decrease in the uncertainty of the initial conditions with increasing number of observations for a simple chaotic system.

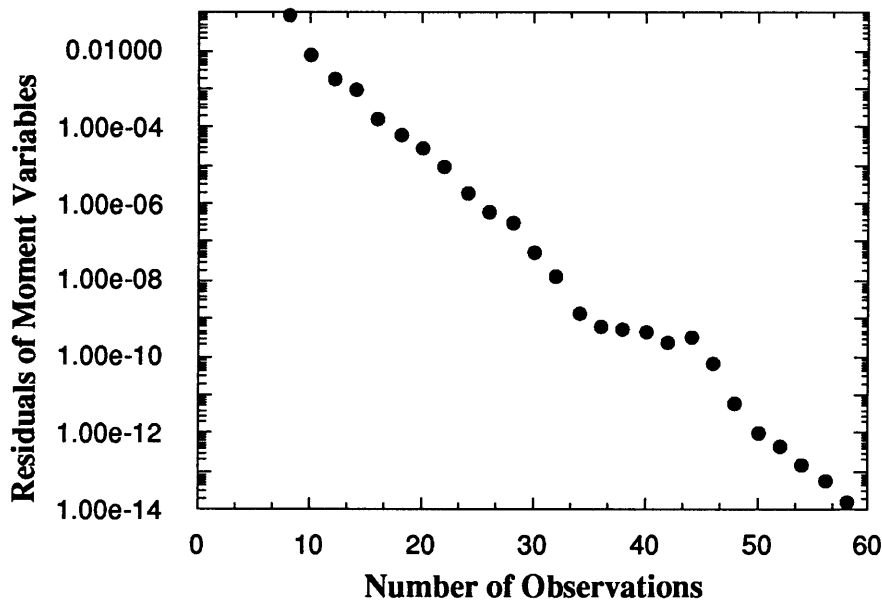## Decrease of Uncertainty with increasing Observations

Figure 15.   There is a dramatic decrease in the uncertainty of initial conditions as exemplified by the decrease in the residuals of the moment variables for this Hyperion test system.

Phase space for the Hyperion system consists of 10 dimensions: the three spatial angles, the three angular velocities, the two principal moments of inertia ratios, the phase slope parameter, G, and the mean opposition magnitude, H. How finely the phase space needs to be searched to find a "close" initial condition is a difficult problem because of the inherent complexity of the phase space. To estimate the necessary sampling, an initial condition is chosen and one dimension of phase space is varied while the other dimensions are held constant at their known values, as in Figure 14. The resulting lightcurves can then be used to examined to determine the sampling interval.

In Figure 14, for example, if all of the other state variables were known exactly, the necessary sampling would be once every 0.7 (dimensionless) rotations per orbit, the

approximate turnover point of the section (dashed) curve. This should be contrasted with a sampling of less than 0.1 if the entire section were used. Since there are eight state variables, this corresponds to a savings of a factor of approximately $7^8 \approx 10^6$ integrations. This assumes the ratio of 7 to 1 will be found in the angular and moment state variables, but serves as a useful illustration of using a section instead of the entire lightcurve. Since this is a simplified one-dimensional analog of the multi-dimensional task, a sampling interval less than 0.7 will be used for the fitting (see next subsection).

The above procedure was performed using one of the angular state variables instead of a velocity variable to estimate the sampling interval necessary for the angular state variables. In this case, the turnover point was at a displacement of approximately 1.0 (dimensionless) radians. This is shown in Figure 16, a plot similar to Figure 14, but using an angular state variable to be varied instead of one of the velocity variables.

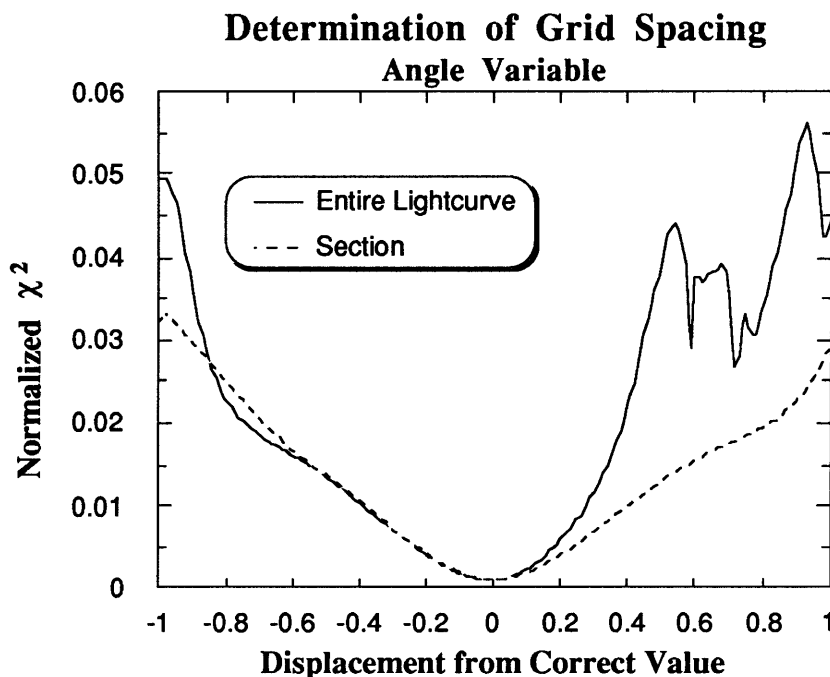## Determination of Grid Spacing
Angle Variable

Figure 16.   A plot similar to Figure 14, but one of the angular variables were varied while the other state variables are held constant. The ordinate and the abscissa are the same as in Figure 14. The section just starts to turn up at a little less than -1 radian. This is an indication of the grid spacing necessary to sample phase space.

Figure 17 is the corresponding plot for the moment ratio variables. The curve is very shallow but is well behaved and indicates that when searching phase space using a section of the lightcurve, the best initial conditions found are not sensitively dependent on the value of the moment ratios. This was indeed found to be the case (see next subsection).

Determination of Grid Spacing
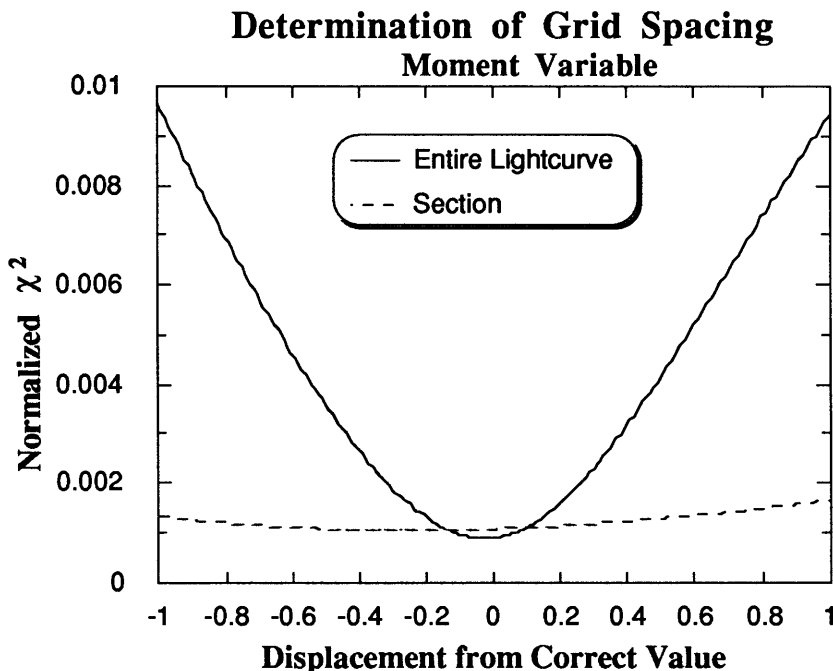### Moment Variable

Figure 17.   A plot similar to Figure 14, but one of the moment ratio variables were varied while the other state variables are held constant. Note that the value of the moment ratio is insensitive to the search for the light curve section but becomes very important for the entire lightcurve.

In addition to the dynamical variables and moment ratios, there are two observational parameters, H and G, which need to be considered when fitting an observed lightcurve. This is because precise values for H and G are not available from the data due to the unknown varying aspect of Hyperion, as discussed in Section IV.

The total number of initial conditions necessary to search all of phase space effectively is calculated by dividing the range of each variable by the grid spacing necessary for that variable. For example, to search the entire range of the angular state variables of 0 to π at a sampling interval of 0.5 radians would require 6 integrations. Since there are three angular state variables, there will be a total of $6^3 \approx 100$ integrations for just the angle variables. Similar considerations apply to the velocity, moment, and H and G variables.

An exhaustive search in which every grid point is integrated over the entire lightcurve, or even a section of the lightcurve, may not be necessary. If using a section of the lightcurve in which the the first point is a maximum or minimum, after correction for phase effects, one or two of the angle variables are constrained to be specific values, thus

reducing the number of grid points necessary to search. To be valid, this technique requires the observation to be a global extremum in which the projected area of the satellite measured is a minimum or a maximum. The minimum or maximum of the lightcurve is not guaranteed to correspond to the maximum or minimum projected area of Hyperion, however, unless the time interval of the observations is large enough to have sampled the satellite from all aspect angles.

In general, the initial condition can be constrained without integrating the equations of motion by comparing the calculated mean opposition magnitude with that measured. If the first magnitude calculated from the projected area is not consistent with the mean opposition magnitude, calculated to be H = 13.81 ± 0.05 (see Section IV), that initial condition is rejected. Most initial conditions can be discarded without any integration of the equations of motion using this comparison. This technique for filtering the grid of initial conditions to be searched is dependent on the first observation and mean opposition magnitude being accurate. To compensate for possible error, one can 1) assign a large uncertainty to the datum, and/or 2) perform the search using a number of different sections.

Even if the first observation is fit by the initial condition, it is possible to prematurely end the integration if it becomes obvious the initial condition is not going to fit the lightcurve. This is done by integrating the initial condition to the time of the second observation in the lightcurve section and comparing the model and observed magnitudes. If they agree to within the uncertainty of the observation and of the mean opposition magnitude, the integration is continued, otherwise the integration is terminated and the next initial condition is checked. To allow for error, this technique requires a large uncertainty be assigned to each point, and/or searching a number of different sections of the lightcurve.

With this sort of filtering, a μVAX can check an average of 320 initial conditions per minute. Thus, searches of thousands of initial conditions can be done in minutes whereas searches of tens of millions of initial conditions can take weeks of computer time. Fortunately, I had weeks of computer time available to search phase space and fit the model to my MHO data.

D. MODEL FITTING TO THE MHO DATA

I performed a search of the above type using six μVAXes over a time interval of a 3-5 weeks. I used four different sections, two of them using slightly different offsets in their searches. In this amount of time, I was able to complete thorough, but not exhaustive, searches of the appropriate areas of phase space. This subsection describes those searches and shows the results.

I searched four sections of the MHO lightcurve with grid spacings of 0.5 radians for the angular state variables, 0.4 for the velocity state variables, and 0.3 for the moment ratios. Except for the moment variables, these values are approximately half the value found from inspection of Figures 14, 16, and 17. There is a trade off between the grid spacing and the amount of computer time, and these values were small enough to adequately search phase space but not so small as to be prohibitively costly in terms of computer time. I searched the entire range of the angular variables from 0 to π. The range searched for the velocity variables was from -3 to 3, discarding all initial conditions in which the sum of the velocity components was greater than the absolute value of three. The range of the moment ratios searched was 0.7 centered on the Duxbury-derived values of A/C = 0.60 and B/C = 0.86 (as reported by Wisdom *et al.* 1984). The range of G searched was 0 to .20 at a sampling of .05, based on how quickly the G parameter varied (see Section IV). The H parameter was calculated from the projected area of the first model point and only those variables which produced a reasonable H were continued. Thus, H was used as a filter as described above. This corresponds to approximately 10 million integrations which can be finished in weeks on a μVAX computer. I assigned a three sigma range on the uncertainty of all observation magnitudes and the mean opposition magnitude, H, to allow for error in the observations, shape and albedo. The programs ran for a total of two to five weeks on each μVAX and wrote the initial conditions which fit greater than eight points to a file. The results of these searches produced initial conditions that typically clumped around a few values.

The initial condition was determined more accurately using the downhill simplex method (see Press *et al.* 1986). This algorithm provides a robust method of finding a minimum in a complex phase space. The simplex method does not use derivatives to find a gradient in phase space, but computes a starting simplex of N+1 dimensions, where N is the number of dimensions searched. The vertices of this simplex are the function to be minimized evaluated at the values supplied as a starting guess. Various geometrical transformations are applied to the vertices of this simplex, such as expanding, contracting, and reflecting, to find the minimum in phase space. The simplex performs these transformations until all the vertices have converged.

The clumps of initial conditions found from the phase-space search were input for the simplex. These clumps typically had the most variation in the moment ratios indicating that I did indeed oversample these state variables. The ambiguity was resolved in the fitting, however, since the lightcurve becomes increasingly sensitive to the moment ratios as the number of observations increase, as can be seen in Figure 17. In all cases, the minimum

found with the simplex fitting technique proved to have a significantly smaller χ^2 than the second best clump of initial conditions found from the search, usually by a factor of two or greater. This was shown by choosing the factor that governs the magnitude of the simplex's geometrical transformation to be small and refitting without the initial condition first found. After the initial simplex fit, another observation point was added to the section of my lightcurve under investigation and the fitting was done on this new section with the simplex algorithm. This procedure was continued until the entire lightcurve was fit, as described in the previous subsection.

Two observations were not included in this fit. One was the observation on day 160 at extremely small solar phase angle, $\alpha = 0.03°$. The phase function used may not fit the opposition surge well, as described in Section III. The other observation omitted from the fit was the one on day 164. It has a formal uncertainty of almost 0.1 magnitude, too large to be meaningful for the fits.

All fits were made unweighted. Except for the observation point noted above, the formal uncertainties were typically of the order 0.01 magnitudes. I assigned a minimum observational uncertainty of 0.01 magnitudes to those observations that had a formal uncertainty smaller than this. At various times in the fitting process, I used the statistical $1/\sigma_i^2$ weighting function and refit. The differences between these and the unweighted fits were negligible for most of the trials. There was virtually no difference between weighted and unweighted fits as the number of observations approached the maximum number, indicating that weighting is unimportant. This is because almost all of the data points have similar uncertainties.

Four different sections, two of them searched twice with different regions of phase spaces, were originally used as data sets to be searched over all of phase space. Two of them differed only in one observation point and these were merged immediately after the phase space search. Two others were terminated during the simplex fitting stage since the fits became very poor in comparison with the other trials as judged from visual inspection of the intermediate lightcurves and comparison of the χ^2. The other three were fit until all points had been added in the manner described above. Of these, two of them had a χ^2 about 50 percent larger than the other one and one of them is included as a comparison to the best fit. Visual inspection of the resulting lightcurve fit confirms that these were much worse than the best one found.

Figure 18 is a plot of the lightcurve, uncorrected for phase effects, with the best fit model superposed. Table VII lists the initial condition used to produce this lightcurve. Note that the values of the state variables are in Wisdom coordinates. The uncertainties in the initial condition were calculated from the covariance matrix of a nonlinear least squares fit to the entire lightcurve (see next section). The numerical value of the first six state variables are, therefore, somewhat arbitrary because these variables would have different values if expressed in Euler coordinates, yet the lightcurve would be the same. The significance of this fit will be discussed in the next section.
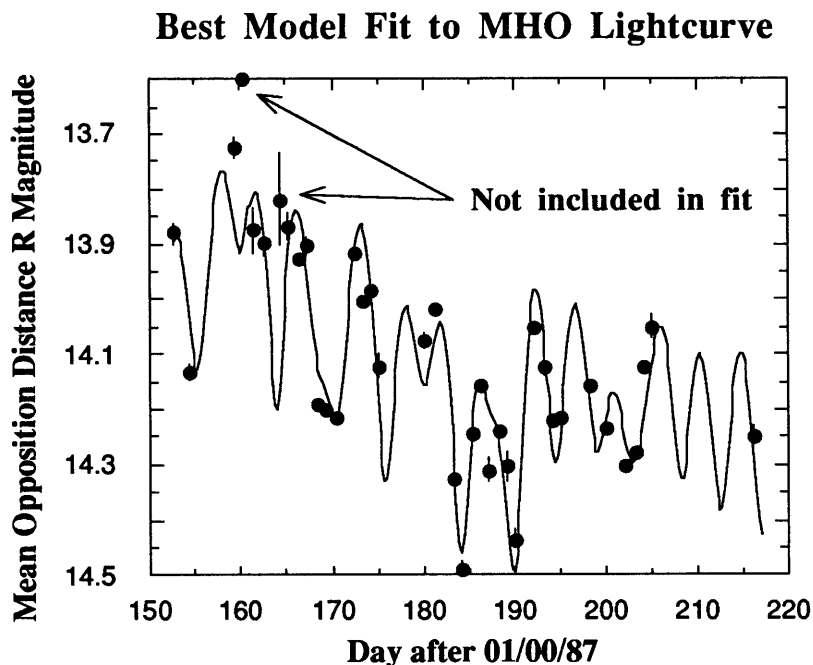
Best Model Fit to MHO Lightcurve

Figure 18.   Best model fit to MHO lightcurve. The points are the measured R magnitudes corrected to mean opposition distance but uncorrected for phase. The solid line is the best model fit obtained with the methods described in the text.

Figure 19 is the second best fit plotted as in Figure 18. Table VII lists the initial conditions for this model fit. As can bee seen by inspection of Figures 18 and 19 or a comparison of χ^2 from Table VIII, this fit is significantly worse than the best fit. This can also be seen from Figure 20 in which the residuals are plotted for both fits. The second best fit is very far away in phase space as can be seen from Table VII. The initial conditions were far enough from each other and phase space is complex enough that these fits did not converge.

Table VII. Initial Condition of Best Fits
(Epoch of 152.444 days after 01/00/87)

Variable	Best	Uncertainty	Second Best
θ	2.881	.13	2.437
φ	0.679	.08	2.991
ψ	1.211	.27	0.426
$\dot{\theta}$	-1.710	.04	1.104
$\dot{\varphi}$	0.009	.26	-2.374
$\dot{\psi}$	1.111	.13	-0.000
A/C	0.533	.05	0.529
B/C	0.782	.09	0.745
G	0.074	.03	0.101
H	13.851	.13	13.853
χ^2	0.144		0.206

Second-Best Model Fit to MHO Lightcurve
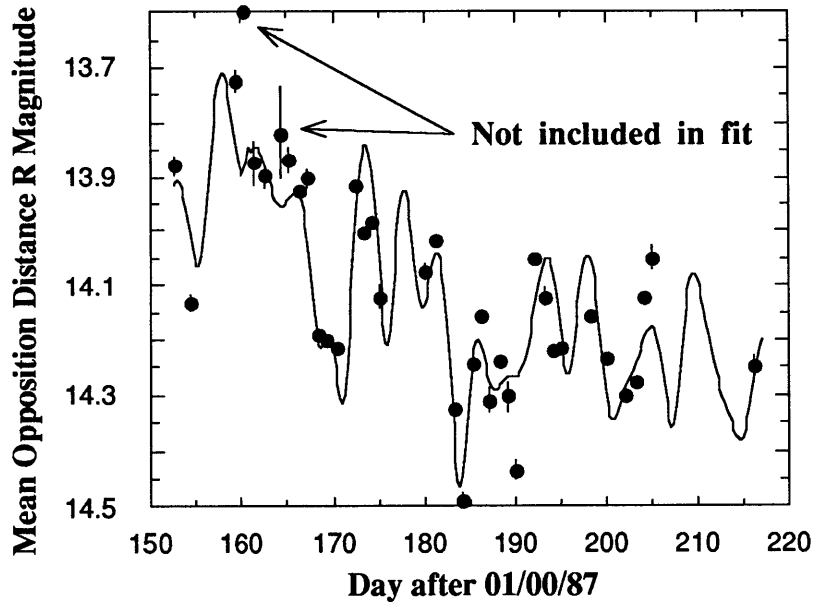
Figure 19. Second best model fit to MHO lightcurve.

Residuals of Model Fits
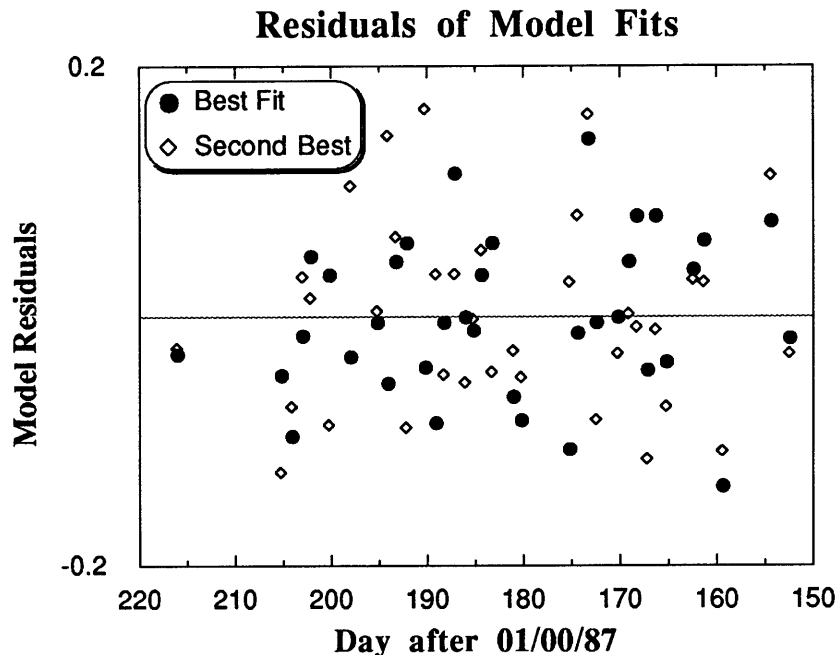

Figure 20.   Residuals to best and second-best model fits. The residuals from the second best fit are typically farther from zero, the horizontal line. There is no apparent correlation in either set of points to indicate any systematic error.

Using a procedure discussed in the last subsection, I was able to fit the model to the observed lightcurve. The best fit is significantly better than the second best fit. The significance of these fits will be discussed in the next section.

C. SUMMARY

In this section I first demonstrated that there was no simple period that could be adequately fit to the MHO lightcurve. For this, I used pdm analysis over a range of two hours to 30 days. Since Hyperion does not appear to be rotating in any periodic state, I proceeded to fit the dynamical model introduced in Section II to the lightcurve. I demonstrated the procedure necessary to convert the dynamical state variables to magnitudes which can be compared to the observed lightcurve. This involved transforming the state variables to an Earth-based frame and determining the projected area of an ellipsoid with those transformed variables. I then showed the proper procedure for fitting to the Hyperion lightcurve using numerical simulations. Counterintuitively, this involves first using only a section of the lightcurve and then adding observations during the final fitting process. Finally, I fit the model to my lightcurve and presented the results. The next section will discuss these procedures and results.

VI. DISCUSSION

Voyager data of Hyperion's shape led Wisdom *et al.* (1984) to predict that Hyperion would be in a rotation state of chaotic tumbling. They first showed that Hyperion's phase space exhibits large scale chaos because of resonance overlap. A surface of section for Hyperion (Figure 4) was calculated by integrating the equations of motion when the satellite was constrained to be have its spin axis perpendicular to the orbital plane. This surface of section clearly shows the large chaotic zone surrounding the synchronous, 1:2, and 2:1 states. These states are attitude unstable and therefore inaccessible as Hyperion tidally evolves through phase space. Numerical simulations indicate that the probability of capture into any of the other resonance states is very small. The full equations of motion of the Hyperion spin-orbit coupling system were integrated by Wisdom *et al.* (1984) and they found all Lyapunov exponents to be nonzero, indicating the system is chaotic.

Hyperion's rotation state has been investigated from ground-based and spacecraft observations. Many of the data sets would have been adequate to determine some commensurate rotation state, but all previous observations of Hyperion were undersampled or had problems with background gradient fitting and subtraction. Peale (1986), Wisdom *et al.* (1984), Wisdom and Peale (1984), and Peale and Wisdom (1984) warn of the possible ambiguities of traditional methods of folding back the lightcurve and performing least-squares analysis on data sampled less than about once every 1.5 days for a chaotically rotating Hyperion. Goguen *et al.* (1983) and Thomas and Veverka (1985) find best-fit periods using this technique. Both fits, however, produce results internally inconsistent with their data sets. Although there have been observations consistent with chaotic rotation, none of the previous observations have been able to definitively constrain the rotation state of Hyperion.

I obtained a lightcurve using the MHO 1.3m and 2.4m telescopes with the MASCOT/MIS detector at the required sampling rate. My lightcurve contains 38 nightly means, an average of nine independent Hyperion observations, over an interval of 64 days (Figure 9). I found that Hyperion is essentially a constant brightness over a period of one night (six hours) and that its color is V–R = 0.41 ± 0.02. The lightcurve amplitude, after correction to mean opposition magnitude (Figure 9), is ≈0.6 magnitudes. This is consistent with the *Voyager*-derived shape.

Using pdm analysis, I demonstrated that no period from 1 hour to 50 days fits the lightcurve. Although a large part of the discussion in Section IV and Section V

concentrated on fitting the H, G phase function to my lightcurve, the essential point is that the analysis is insensitive to the form of the phase correction. This is demonstrated by comparing the pdm plots with phase correction and without phase correction (Figure 10), and noting that the two plots are very similar. Even the best period found from pdm analysis, however, does not fit the data well. This was shown statistically, as well as through inspection of the rotational phase plot (Figure 11).

CCD photometry of Hyperion over an interval of 64 days shows no evidence of periodic modulation in the lightcurve. There are three possible explanations: 1) The motion is simply periodic but I have large, undetected errors in my lightcurve. 2) The motion is periodic in a complicated manner. or 3) The motion is chaotic.

The lightcurve is sound. The stability of Titan, the standard stars, and field stars in the same background gradient as Hyperion provides evidence that all aspects of the data acquisition and reduction are done consistently and correctly. Although it is possible that undetected error can inadvertently be introduced into any data set, I have made certain that any error in my lightcurve is not large enough to invalidate the period-determination analysis.

It is possible to stipulate some unspecified forcing such that Hyperion is in a regular, yet complicated, rotation state consistent with my lightcurve. The object which could have the largest effect on Hyperion, other than Saturn, is Titan. Even at closest approach, however, Titan's gravitational effect is only 3 percent that of Saturn. Tidal effects are an order of magnitude smaller. Integrated over the entire orbit, Titan's interaction would certainly be unable to affect Hyperion's rotation state enough to significantly alter my lightcurve. Any *ad hoc* forcing without a physical basis does not deserve serious consideration without further evidence.

No periodicities were found that adequately described my lightcurve. Is this conclusion equivalent to Hyperion being chaotic? Chaos has a very specific definition (given in Section II): chaotic motion is deterministic but unpredictable motion due to exponential divergence of nearby initial conditions. The equations of motion are known for the Hyperion spin-orbit coupling problem. Thus, the motion is deterministic: if a well-defined initial condition is given, the rotation state at any other time can, in principle, be calculated. Even infinitesimal uncertainties, however, limit this predictive ability. It is the exponential divergence of nearby initial conditions which gives chaotic systems their apparent random nature. While this work does not, and cannot, *prove* Hyperion is in a chaotic rotation state, it is very strong circumstantial evidence that Hyperion is tumbling

chaotically. This is the only data set from which this can be stated with conviction because of the problems with previous observations/analyses and because this is a high-quality, well-sampled lightcurve. *Voyager 2,* in addition to determining the size and shape of Hyperion, found the orientation of this satellite to be with its spin axis nearly parallel to the orbital plane (Thomas and Veverka 1985). This orientation would be difficult to reconcile with any regular rotation state.

Various modifications to the dynamical model presented in Section II were introduced in the last section to account for the observational details of the lightcurve. The time of the observations were corrected for light travel time. This allowed the true position of Hyperion in its orbit at any particular time to be calculated from its orbital elements. I then demonstrated the procedure necessary to calculate the relative magnitude of an observation based on its rotation state. This involved transforming the spatial coordinates to a geocentric system and converting the projected area of the ellipsoid to a magnitude.

Numerical simulations allowed me to determine the best method of fitting the model to a lightcurve. Finding the initial conditions is a two step process. First, a well-sampled section of the lightcurve is used to find the general area of phase space corresponding to the true initial conditions. The model should then be fit to the section and the rest of the observations should be added singly, fit again, and so on, until all observations are fit.

Phase space becomes increasingly complex as the number of observations increases. This suggests that a search of phase space by a well-sampled section of the lightcurve should be used to determine an approximation to the initial condition. For most applications, it is usually best to gather as much data as possible and then do whatever fitting is necessary. For a chaotic system, this may not be the best strategy. Consider, for example, fitting the model to one observation: there are a number of initial conditions scattered throughout phase space which would fit the datum. If the next observation is added, there are fewer initial conditions which will fit the data, but there will be more nearby initial conditions that are in the process of diverging. As more observations are added, it is obvious that the number of initial conditions that approximate the data will decrease, but their surroundings in phase space will get increasingly complex, with some initial conditions approximating the data and most quickly diverging. This would not be the case for a dynamically regular system.

After the approximate initial condition is found, the lightcurve section can then be fit with some minimization routine to better define the initial condition. The next point in the lightcurve should then be added and the initial conditions for this new section fit. This procedure continues until the model has been fit to the entire lightcurve. Such a technique

has used been successfully for a simulated Hyperion data set (Klavetter 1985, unpublished) and a simple chaotic system (Wisdom 1987; Chakrabarty 1988, unpublished). In contrast with the usual $1/\sqrt{N}$ decrease in the uncertainty of the initial condition expected from elementary statistics, these studies found that when fitting to chaotic trajectories an exponential decrease in the uncertainties was found. Noting the definition of chaos, it makes sense that this should be so. As the number of observations increases, two rotation states that were initially close together and fit the first part of the lightcurve would begin to diverge and only one would fit the rest of the lightcurve well. My numerical simulations indicate that when a data set spans an interval of time on the same order as my lightcurve, the initial conditions can be determined with high precision. It is ironic that the chaotic nature which would allow me to determine the rotation state to a very high precision, if I could determine the approximate initial condition, makes it very difficult to find that approximate initial condition.

The best lightcurve presented in the last section (Figure 18) demonstrates the sort of results obtainable when phase space is searched at the resolution given in Section V. The major question is how good is the fit?

One measure of the significance of the fit is to compare the internal uncertainties with the measured χ^2, the sum of the observed minus the calculated magnitudes. For a good fit, the square root of χ^2 normalized by the number of observations would be approximately equal to the measured uncertainties. For the best lightcurve shown in Figure 18, $\sqrt{(\chi^2/N)} = 0.06$, where N = 36 is the number of observations. The measured uncertainties include a combination of the observational uncertainty, typically $\sigma_o \approx 0.02$, the uncertainty in Hyperion's shape, $\sigma_s \approx 0.03$, and the uncertainty in Hyperion's albedo variation, $\sigma_a \approx 0.01$ (the shape and albedo uncertainties will be discussed below). Thus, the total uncertainty is $\sigma_T \approx 0.04$, not too much less than the model uncertainty of 0.06. Inspection of Figure 18 confirms that the fit is not unreasonable. Given the uncertainties inherent with the present precision of Hyperion's shape and albedo, this may be the best fit possible.

My search of phase space and subsequent fitting determined the rotation state of Hyperion, including the two principal moment of inertia ratios. Due to the chaotic nature of the system, however, all dynamical information contained in the state variables would be lost on the order of two Hyperion orbital periods (Wisdom et al. 1984). Thus, the rotation state would not be known now even if I had obtained a precise fit to my lightcurve with no errors in shape and albedo. This demonstrates that it would be futile to try and combine all Hyperion measurements made over time intervals greater than approximately 40 days. The moment ratios,however, can provide information on Hyperion's internal structure.

Using the best fit ellipsoid to *Voyager* data, Duxbury (as reported in Wisdom *et al.* 1984) found the following values for the principal semi-axes:

$$a = 190 \quad km$$
$$b = 145 \quad km$$
$$c = 114 \quad km$$

with an uncertainty of 15 km. The moment ratios and their formal uncertainties are

$$\frac{A}{C} = 0.60 \pm 0.122$$

$$\frac{B}{C} = 0.86 \pm 0.159 \ .$$

These values are consistent with the best model fit values of A/C = 0.54 ± 0.05 and B/C = 0.79 ± 0.09. The uncertainties of the moment ratios are large for both the *Voyager*-derived values and my fitted values. However, my fits are consistent with the *Voyager* values, indicating that Hyperion is not grossly inhomogeneous if the fit is valid. Furthermore, my fits indicate there is no reason to assume that Hyperion does not have a uniform mass distribution.

The simplex routine does not produce any formal errors, as I have listed in Table VII. After I had found the initial condition using the techniques described, I numerically calculated the derivatives necessary to refit the entire lightcurve using nonlinear least-squares techniques. This was possible since I had already fit for the best answer. The least-squares answer did not give me any more information about the rotation state, but inversion of the covariance matrix yields formal uncertainties based on the data. These are the uncertainties listed in Table VII. In addition, correlation coefficients were calculated and it was found, not surprisingly, that there were strong correlations among the angular variables, among the velocity variables, and between the moment variables ($\approx$ 0.7 - 0.9) but very small correlation coefficients between the three different sets of variables. Furthermore, there was little correlation between the state variables and the H, G parameters, but the H and G variables were highly correlated. Considering how these variables enter the equations of motion and how they are used to calculate the model magnitudes, this is not unexpected. The least-squares technique also played a sort of check on various aspects of the computer code.

There are other effects that could hinder any sort of fitting algorithm. Inspection of Figure 8 shows that data at solar phase angles $\alpha \geq 0.3°$ are described adequately by the H, G phase function, within the uncertainties due to the aspect of Hyperion, as described in Section IV. The opposition surge, however, may not be fit well with this phase function. This is why I did not include the observation nearest opposition in my model fitting. It is possible to separate the phase effect from the rotational effect, however, by simultaneously fitting the dynamical model and the chosen phase function to the lightcurve. For the best model fit, the slope parameter, $G = 0.074 \pm 0.03$, is consistent with the observationally fitted value of $G = 0.056 \pm 0.14$. Thus, it appears as if the slope parameter is less than the expected value for C-type asteroids.

Thomas and Veverka (1985) report that any albedo variations are "mostly averaged out over the disk." This is confirmed by an inspection of Figure 1, one of the highest resolution images obtained by *Voyager 2*. To quantify the variation in Hyperion's albedo, I measured the mean signal in a 10 x 10 box placed at 5 separated places on the disk of the Hyperion image shown in Figure 1. The results are listed in Table VIII. The mean varies by less than the standard deviation of about 3 ADUs. From this image, it appears as if albedo variations are indeed small when averaged over the disk. There is about a 1% mean variation, thus $\sigma_a \approx 0.01$.

Table VIII. Hyperion Albedo Variations

Relative Location	Mean of 100 pixels	Standard Deviation
75, 57	40.02	4.00
58, 75	43.89	2.99
70, 63	40.12	3.05
64, 80	39.98	4.44
81, 64	40.88	3.61

The largest uncertainty in the model is Hyperion's shape. Figure 21 is a *Voyager* image of Hyperion which presents a view that does not approximate an ellipsoid. Thomas and Veverka (1985) note that Hyperion "cannot be described well by an ellipsoid." Thomas *et al.* (1986) plot the deviations of Hyperion's limb from a best-fit ellipse over about 160° of arc. They find variations of up to ±10 percent for specific places along the limb with a mean deviation of approximately 3–5 percent. Without a greater coverage of Hyperion's topography from spacecraft observations, it is impossible to rigorously asses the problems this will cause any model fitting algorithm.
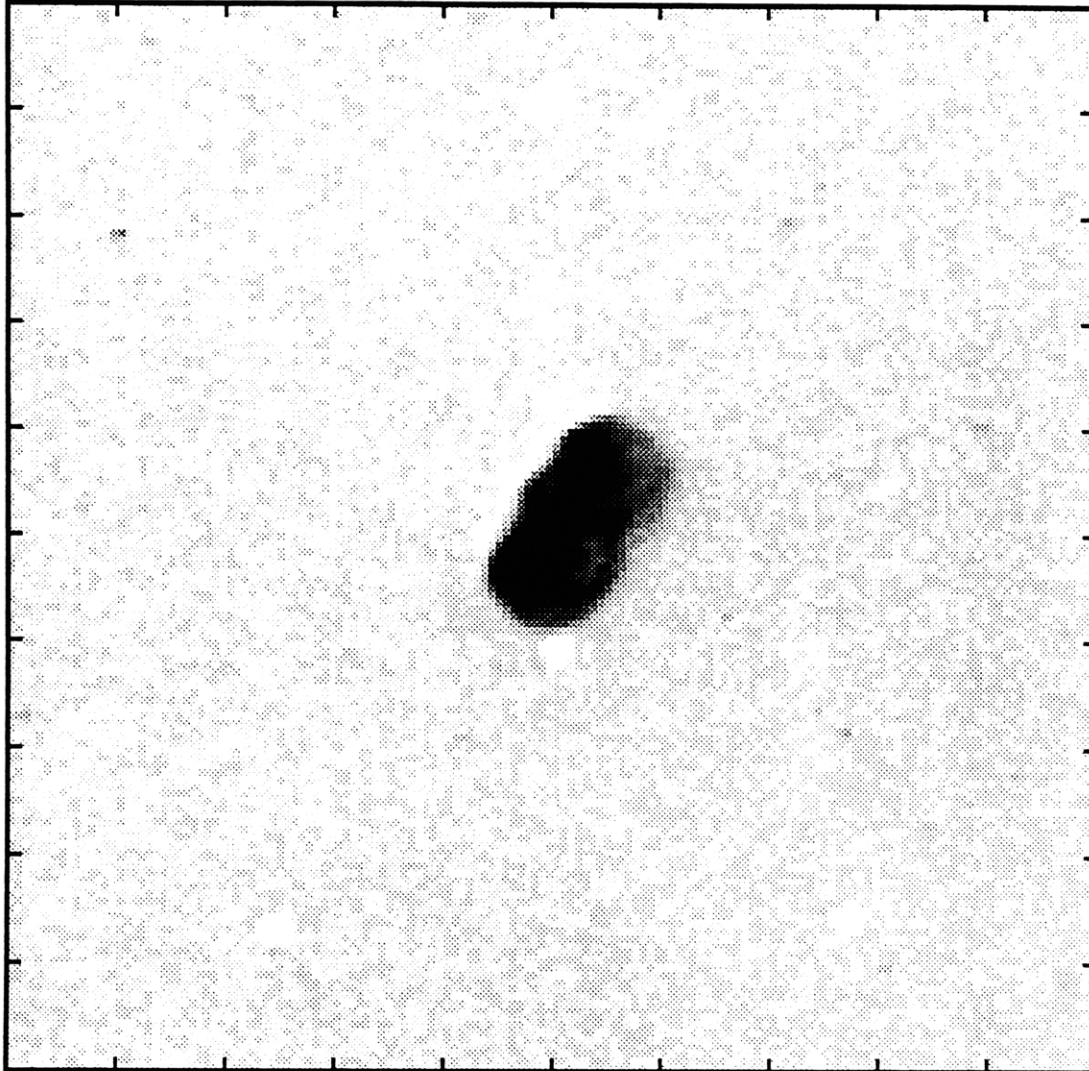
Figure 21.   Another high resolution *Voyager* image (see Figure 1). This one, however does not appear to approximate an ellipse in cross section.

Numerical simulations indicate that model fitting can still be successful for reasonable errors in the ellipsoid's shape. Figure 22 is a plot of the error in the ellipsoid shape versus the residuals to the lightcurve. For this figure, a lightcurve was generated with a known initial condition and a gaussian error of the specified amount was added to each observation. The model was then fit to the lightcurve using the known initial condition as a starting guess for the simplex algorithm. The residuals were calculated by taking the square root of the sum of the squares of the individual differences between the fitted initial conditions and the known initial conditions used to generate the lightcurve. There is a roughly linear relationship between the amount of error and the residuals. The fitted initial conditions remain relatively near the true value. Thus, if the approximate initial condition can be found, even shape errors as large as 8–10 percent will still allow an accurate determination of the initial conditions to be made, but the results will be less precise. This simulation does not indicate if a general search of phase space will find the known initial condition, but the residuals are small for errors of about 3–5 percent and should not affect the general search of phase space.

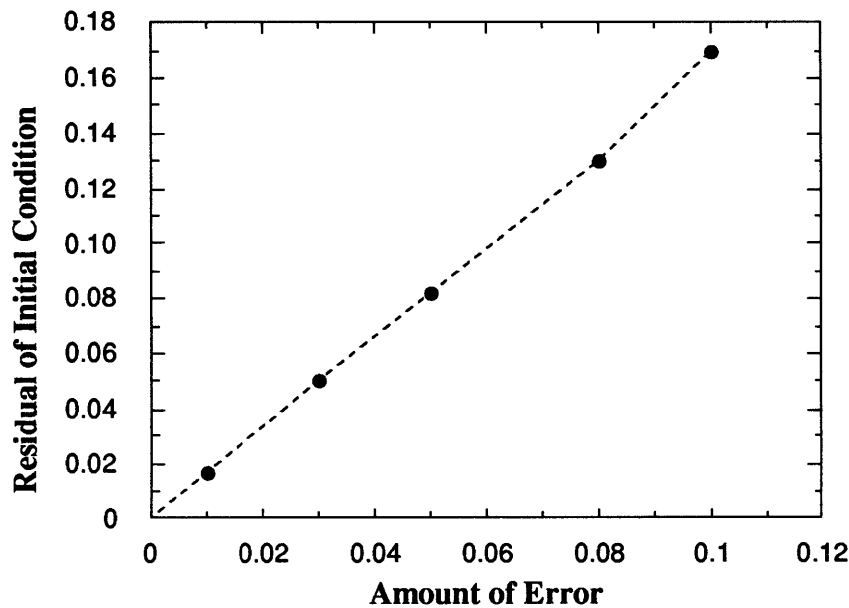## Effect of Shape Error on Initial Condition

Figure 22.   Lightcurves were generated for one initial condition with varying amounts of gaussian error added to each observation to simulate shape errors. The difference between the fitted initial condition and the true initial condition, calculated as the root of the sum of the normalized χ^2, is plotted on the ordinate. The dotted line connects the individual points.

The motion of Hyperion is independent of the details of its shape. The equations of motion depend on the principal moments of inertia, and not explicitly on the shape. The same motion would be observed for a homogeneous ellipsoid and a sphere whose mass

distribution was such that both objects had the same values for the principal moments of inertia. The connection between shape and moments of inertia is that the moments are estimated from the shape for a body of homogeneous composition. The only parameter in the model that is explicitly dependent on the shape is the projected area of the ellipsoid, and thus the relative magnitude. Errors propagated to the relative magnitudes, however, will be less pronounced

Deviations of the amount shown by Thomas *et al.* (1986) would typically affect the projected area, and thus relative magnitude, of Hyperion by ≤3–4 percent. From Figure 22, it is seen that this is about a 5 percent error in the initial conditions. This is the maximum precision that could be expected from perfect data and precise fitting.

Does my fitted lightcurve represent the best possible fit to the data? Only a rigorous search of phase space at better sampling can answer this question. However, the best model fit lightcurve does a pretty good job of fitting the data, as can be seen by inspection of Figure 19 and the comparison of uncertainties noted above. It is not bothersome that the second-best model fit does not coincide with the first. Due to the nature of fitting to chaotic motion, once the fit starts off in some slightly wrong direction, it can keep going so far as to never get back to the correct answer. This was seen in various numerical simulations I performed. In addition, inspection of the lightcurve and residuals show that it is not a good fit. For the second-best fit, the lightcurve uncertainty is 0.08, a factor of 2 greater than the expected uncertainty.

So it is impossible to say with my present resources and data if I have found the "true" initial condition, but based on my numerical simulations I have marginally sampled phase space at the required sampling to find the correct initial condition. However, even with adequate sampling, the initial condition could still possible "fall through the cracks." Furthermore, given the uncertainties in Hyperion's shape, it may be impossible to fit the model to my MHO lightcurve. Based on my numerical simulations, however, it appears possible to do the fit. The results produced by following my procedure yield reasonable values for the moment ratios, consistent with Hyperion having a uniform density.

VII. CONCLUSIONS

A. Observational

1. Hyperion is not in any regular/periodic rotation state.
2. Hyperion exhibits a strong brightness variation with phase, including an opposition surge of approximately 0.3 magnitudes at solar phase angles of less than about 0.3°. The numbers are imprecise because of the rotational effects.
3. Hyperion varies less than 0.01 magnitude over timescales of less than six hours.
4. The color of Hyperion is $V - R = 0.41 \pm 0.02$.

B. Dynamical

1. To find the approximate initial condition, it is better to search phase space with a well-sampled section of the lightcurve than the entire lightcurve. I do not know if this is a general result that could be related to all chaotic systems.
2. If the approximate initial condition could be found via the exhaustive search of phase space or some other method, the section of the lightcurve could be fit, the next observation added, fit again, and so on until the true initial condition was found. There would be an exponential decrease in the uncertainty of the rotation state and the principal moments of inertia. There will be some limit due to the uncertainty of Hyperion's shape. This exponential decrease in the uncertainties of the initial conditions could be a general feature of chaotic systems.
3. Best fitted values of the Hyperion moment ratios are consistent with Hyperion being a body with a uniform mass distribution.

REFERENCES

Andersson, L. E. 1974. A Photometric study of Pluto and Satellites of the Outer Planets. Ph.D. thesis, University of Indiana, Bloomington.

Andersson, L. E. 1977. Variability of Titan: 1896-1974. In *Planetary Satellites,* ed. J. A. Burns (Tucson: Univ. of Arizona Press), p. 451-462.

Binzel, R., Green, J., and Opal, C. 1986. Chaotic Rotation of Hyperion? *Nature.* **320**:511.

Bowell, E., Harris, A., and Lumme, K. 1987. A Two-Parameter Magnitude System for Asteroids. Submitted to *Icarus.*

Burns, J. A. Some Background About Satellites. In *Satellites,* eds. J. A. Burns and M. S. Matthews (Tucson: Univ. of Arizona Press), pp. 1-38.

Chakrabarty, D. 1988. Determination of Initial Conditions for Chaotic Systems: Numerical Studies of the Standard Mapping. Unpublished.

Chapman, C. R., and McKinnon, W. B. Cratering of Planetary Satellites. In *Satellites,* eds. J. A. Burns and M. S. Matthews (Tucson: Univ. of Arizona Press), pp. 492-580.

Chirikov, B. V. 1979. A universal instability of many-dimensional oscillators systems. Phys. Rep. **52**:263-379.

Clark, R. N., Brown, R. H., Owensby, P. D., and Steele, A. 1984. Saturn's Satellites: Near-Infrared Spectrophotometry (0.65-2.5 μm) of the Leading and Trailing sides and Compositional Implications. *Icarus.* **58**:265-281.

Conner, S. 1984. Photometry of Hyperion. M.S. Thesis, Massachusetts Institute of Technology.

Cruikshank, D. P. 1979. The Surfaces and Interiors of Saturn's Satellites. *Reviews of Geophysics and Space Physics.* **17**:165-176.

Cruikshank, D. P., Bell, J. F., Gaffey, M. J., Brown, R. H., Howell, R., Beerman, C., and Rognstad, M. 1983. The Dark Side of Iapetus. *Icarus.* **53**:90-104.

Cruikshank, D. P., and Brown, R. H. 1982. Surface Composition and Radius of Hyperion. *Icarus*. **50**:82-87.

Degewij, J., Andersson, L. E., and Zellner, B. 1980. Photometric Properties of Outer Planetary Satellites. *Icarus*. **44**:520-540.

Franklin, F. A., and Cook, A. F. 1974. Photometry of Saturn's Satellites: The opposition effect of Iapetus at maximum light and the variability of Titan. *Icarus*. **23**:355-362.

Franz, O., and Millis, R. 1971. A Search for an Anomalous Brightening of Io after Eclipse. *Icarus*. **14**:13-15.

Goguen, J. 1986. Personal communication.

Goguen, J., Cruikshank, D. P., Hammel, H., and Hartmann, W. K. 1983. The rotational lightcurve of Hyperion during 1983. *Bull. Amer. Astron. Soc.* **15**:854.

Goldreich, P., and Peale, S. 1966. Spin-Orbit coupling in the Solar System. *Astron. J.* **71**:425-438.

Goldstein, H. 1981. *Classical Mechanics*. Addison-Wesley, Reading.

Harris, D. L. 1961. Photometry and colorimetry of planets and satellites. In *Planets and Satellites* (G. Kuiper and B. Middlehurst, Eds.). pp. 272-342. Univ. of Chicago Press, Chicago.

Hendon, A., and Kaitchuck, R. 1982. *Astronomical Photometry* (New York: Van Nostrand Reinhold Company Inc.).

Hénon, M. and Heiles, C. 1964. The applicability of the third integral of motion: Some numerical experiments. *Astron J.* **69**:73-79.

Klavetter, J. J. 1985. Observational Evidence of Hyperion's Chaotic Tumbling: Determination of Initial Conditions. Unpublished.

Klavetter, J. J. 1989. Rotation of Hyperion: I. Observations. *Astron J.* February 1989.

Kruper, J. 1987. Personal communication.

Landolt, A. 1983. UBVRI Photometric Standard Stars Around the Celestial Equator. *Astron. J.* **88**:439-460.

Meyer, S. and Ricker, G. 1980. A Dual CCD, Astronomical Spectrometer and Direct Imaging Camera. *S.P.I.E. Proc.* **264**:38.

Noland, M., Veverka, J., Morrison, D., Cruikshank, D., Lazarewicz, A., Morrison, N., Elliot, J., Goguen, J., and Burns, A. 1974. Six-color Photometry of Iapetus, Titan, Rhea, Dione and Tethys. *Icarus.* **23**:334-354.

Peale, S. 1977. Rotational Histories of the Natural Satellites. In *Planetary Satellites,* ed. J. A. Burns (Tucson: Univ. of Arizona Press), pp. 87-112.

Peale, S. 1986. Orbital Resonances, Unusual Configurations, and Exotic Rotation States Among the Planetary Satellites. In *Satellites,* eds. J. A. Burns and M. S. Matthews (Tucson: Univ. of Arizona Press), pp. 159-223.

Peale, S. and Wisdom, J. 1984. Do Current Observations Support the Hypothesis of Chaotic Rotation for Hyperion? *Bull. Amer. Astron. Soc.* **16**:686-7.

Press, W. H., Flannery, B. P., Teukolsky, S. A., and Vetterling, W. T. 1986. *Numerical Recipes*(Cambridge: Cambridge University Press).

Smith, B. A., Soderblom, L., Batson, R., Bridges, P., Inge, J., Masursky, H., Shoemaker, E., Beebe, R., Boyce, J., Briggs, G., Bunker, A., Collins, S. A., Hansen, C. J., Johnson, T. V., Mitchell, J. L., Terrile, R. J., Cook., A. F., Cuzzi, J., Pollack, J. P., Danielson, G. E., Ingersoll, A. P., Strom, M. E., Suomi, V. E. 1982. A new look at the Saturn system: The *Voyager 2* images. *Science.* **215**:504-537.

Stellingwerf, R. 1978. Period Determination Using Phase Dispersion Minimization. *Astrophys. J.* **224**:953-960.

Stetson, P. 1987. DAOPHOT: A Computer Program for Crowded-Field Stellar Photometry. *Pub. Astron. Soc. Pacific.* **99**:191-222.

Tholen, D. J., and Zellner, B. 1983. Eight color photometry of Hyperion, Iapetus, and Phoebe. *Icarus*. **53**:341-347.

Thomas, G. B., and Finney, R. L. 1980. Calculus and Analytic Geometry. (Reading, Massachusetts: Addison-Wesley).

Thomas, P., and Veverka, J. 1985. Hyperion: Analysis of *Voyager* Observations. *Icarus*. **64**:414-424.

Thomas, P., Veverka, J., Dermott, S. Small Satellites. In *Satellites,* eds. J. A. Burns and M. S. Matthews (Tucson: Univ. of Arizona Press), pp. 802-835.

Thomas, P., Veverka, J., Morrison, D., Davies, M., and Johnson, T. V. 1983. Saturn's small satellites: *Voyager* imaging Results. *J. Geophys. Res.* **88**:8743-8754.

Thomas, P., Veverka, J., Wenkert, D., Danielson, G., and Davies, M. 1984. Hyperion: 13-day Rotation from *Voyager* Data. *Nature*. **307**:716-717.

Tody, D. 1986. The IRAF Data Reduction and Analysis System. *S.P.I.E.* **627**:627-91.

Wisdom, J. 1983. Chaotic behavior and the origin of the 3/1 Kirkwood gap. *Icarus*. **56**:51-74.

Wisdom, J. 1987. Urey Prize Lecture: Chaotic Dynamics in the Solar System. *Icarus*. **72**:241-275.

Wisdom, J. and Peale, S. 1984. The Light Curve of Hyperion. *Bull. Amer. Astron. Soc.* **16**:707.

Wisdom, J., Peale, S., and Mignard, F. 1984. The Chaotic Rotation of Hyperion. *Icarus*. **58**:137-152.

Woltjer, J. 1928. *Annalen van de Sterrewacht te Leiden.* **16**:64.

APPENDIX A
Derivation of the Transformation Matrix

The transformation matrix $\mathbf{A}$ defined by $\vec{x} = \mathbf{A}\vec{x}'$, where the primed coordinates are the body axes and the unprimed coordinates are the Saturnocentric axes, is a combination of the three simple rotations described in Section II. These rotations are actually transforming from the Saturnocentric axes to the body axes through the three Euler angles such that $\mathbf{A}^{-1} = \mathbf{BCD}$ where the three rotations defining the Euler angles are

$$\mathbf{D} = \begin{bmatrix} \cos\theta & \sin\theta & 0 \\ -\sin\theta & \cos\theta & 0 \\ 0 & 0 & 1 \end{bmatrix}$$

$$\mathbf{C} = \begin{bmatrix} 1 & 0 & 0 \\ 0 & \cos\varphi & \sin\varphi \\ 0 & -\sin\varphi & \cos\varphi \end{bmatrix}$$

$$\mathbf{B} = \begin{bmatrix} \cos\psi & \sin\psi & 0 \\ -\sin\psi & \cos\psi & 0 \\ 0 & 0 & 1 \end{bmatrix},$$

as described in Section II. It should be noted that the Saturnocentric coordinate system is inertial and is defined by Hyperion's orbit at periapse. Performing the above rotations in this order produces

$$\mathbf{A}^{-1} = \begin{bmatrix} \cos\theta\cos\psi - \sin\theta\cos\varphi\sin\psi & \sin\theta\cos\psi + \cos\theta\cos\varphi\sin\psi & \sin\varphi\sin\psi \\ -\cos\theta\sin\psi - \sin\theta\cos\varphi\cos\psi & -\sin\theta\sin\psi + \cos\theta\cos\varphi\cos\psi & \sin\varphi\cos\psi \\ \sin\theta\sin\varphi & -\cos\theta\sin\varphi & \cos\varphi \end{bmatrix}$$

such that $\mathbf{A}^{-1}$ is the inverse of $\mathbf{A}$ defined above. Since $\mathbf{A}^{-1}$ is a product of simple rotation matrices, $\mathbf{A}^{-1} = \mathbf{A}^{T}$ (Goldstein 1981). $\mathbf{A}$ is the transpose of the matrix above:

$$\mathbf{A} = \begin{bmatrix} \cos\theta\cos\psi - \sin\theta\cos\varphi\sin\psi & -\cos\theta\sin\psi - \sin\theta\cos\varphi\cos\psi & \sin\theta\sin\varphi \\ \sin\theta\cos\psi + \cos\theta\cos\varphi\sin\psi & -\sin\theta\sin\psi + \cos\theta\cos\varphi\cos\psi & -\cos\theta\sin\varphi \\ \sin\varphi\sin\psi & \sin\varphi\cos\psi & \cos\varphi \end{bmatrix}.$$

The Wisdom coordinates are similar to the Euler coordinates except the third rotation is

$$\mathbf{B}^w = \begin{bmatrix} \cos\psi & 0 & -\sin\psi \\ 0 & 1 & 0 \\ \sin\psi & 0 & \cos\psi \end{bmatrix}$$

where the superscript denotes that this is a rotation matrix for the Wisdom coordinates. For this set of rotations, the transformation matrix is

$$\mathbf{A}^w = \begin{bmatrix} \cos\theta\cos\psi - \sin\theta\cos\varphi\sin\psi & -\sin\theta\cos\varphi & \cos\theta\sin\psi + \sin\theta\sin\varphi\cos\psi \\ \sin\theta\cos\psi + \cos\theta\sin\varphi\sin\psi & \cos\theta\cos\varphi & \sin\theta\sin\psi - \cos\theta\sin\varphi\cos\psi \\ -\cos\varphi\sin\psi & \sin\varphi & \cos\varphi\cos\psi \end{bmatrix}$$

where the angles are now in Wisdom coordinates.

If the orientation of the satellite with respect to the planet is required, the above needs to be modified. $\theta - f$ is angle between the ellipsoid's long axis and the satellite to planet line. This is not necessary for any of the transformations discussed in this work.

These transformation matrices will be used in the calculation of the direction cosines, the calculation of projected area, and in converting coordinate systems which will be described in following appendices.

APPENDIX B
Derivation of angular velocity in Euler coordinates

In Section II, the angles of the Euler coordinate system were defined. When θ, φ, and ψ change with time, the angular velocities associated with these angle will be about the axes shown in Figure 3 (Section II) such that $\vec{\omega} = \dot{\theta}\hat{z} + \dot{\varphi}\hat{x}' + \dot{\psi}\hat{c}$. This is easily seen by setting any two of the angular velocities zero and noting about which axis the third is rotating. The derivation of the equations of motion in Section II and Appendix D requires $\vec{\omega} = \omega_a\hat{a} + \omega_b\hat{b} + \omega_c\hat{c}$. The transformation between the dynamical state variables and the components of ω will be derived in this appendix.

The first intermediate axes are

$$\hat{x}' = \hat{a}\cos\psi - \hat{b}\sin\psi$$
$$\hat{y}' = \hat{a}\sin\psi + \hat{b}\cos\psi$$

and

$$\hat{z} = \hat{c}\cos\varphi + \hat{y}'\sin\varphi.$$

Substituting for $\hat{y}'$:

$$\hat{z} = \hat{a}\sin\varphi\sin\psi + \hat{b}\sin\varphi\cos\psi + \hat{c}\cos\varphi.$$

Now everything can be described in terms of the body axes. Final substitution produces

$$\omega_a = \dot{\theta}\sin\varphi\sin\psi + \dot{\varphi}\cos\psi$$
$$\omega_b = \dot{\theta}\sin\varphi\cos\psi - \dot{\varphi}\sin\psi$$
$$\omega_c = \dot{\theta}\cos\varphi + \dot{\psi}$$

as in Section II. The derivation in Wisdom coordinates proceeds along similar lines and the angular velocities in this case are

$$\omega_a^w = -\dot{\theta} \cos \varphi \sin \psi + \dot{\varphi} \cos \psi$$

$$\omega_b^w = \dot{\theta} \sin \varphi + \dot{\psi}$$

$$\omega_c^w = \dot{\theta} \cos \varphi \cos \psi + \dot{\varphi} \sin \psi.$$

APPENDIX C
Calculation of direction cosines

The direction cosines are needed to specify the equations of motion, as described in Section II and Appendix D. Direction cosines are defined as

$$\alpha \equiv \hat{x} \cdot \hat{a}$$
$$\beta \equiv \hat{x} \cdot \hat{b}$$
$$\gamma \equiv \hat{x} \cdot \hat{c}$$

where $\hat{x}$ is the planet to satellite unit vector, as defined in Section V, and a, b, and c are the body axes. As in Section V, let the body axes be noted by a primed coordinate system such that

$$\alpha = \hat{x} \cdot \hat{x}'$$
$$\beta = \hat{x} \cdot \hat{y}'$$
$$\gamma = \hat{x} \cdot \hat{z}'.$$

As noted in Section V, $\vec{x} = \mathbf{A}\vec{x}'$ so the direction cosines are merely the matrix elements

$$\alpha = A_{11}$$
$$\beta = A_{12}$$
$$\gamma = A_{13}.$$

Referring to the transformation matrix in Appendix A, the direction cosines are

$$\alpha = \cos(\theta - f)\cos\psi - \sin(\theta - f)\cos\varphi \sin\psi$$
$$\beta = -\cos(\theta - f)\sin\psi - \sin(\theta - f)\cos\varphi \cos\psi \qquad (3)$$
$$\gamma = \sin(\theta - f)\sin\varphi$$

Similarly for the direction cosines in Wisdom coordinates

$$\alpha = A^{w}_{11}$$
$$\beta = A^{w}_{12}$$
$$\gamma = A^{w}_{13},$$

where the superscript signifies the transformation matrix is in the Wisdom coordinates. Again, referring to Appendix A, the direction cosines in these coordinates

$$\alpha^w = \cos(\theta - f)\cos\psi - \sin(\theta - f)\sin\varphi\sin\psi$$
$$\beta^w = -\sin(\theta - f)\cos\varphi$$
$$\gamma^w = \cos(\theta - f)\sin\psi + \sin(\theta - f)\sin\varphi\cos\psi$$

where the rotation angles are now understood to be the Wisdom coordinates, as defined in Section II and Appendix A.

APPENDIX D
Equations of Motion

In Section II, I outlined the derivation of the equations of motion in Euler coordinates. In this appendix, the details of this derivation will be given as well as the full equations of motion.

As shown in Section II, the Euler equations for the spin-orbit coupling system of the Hyperion model considered are

$$A\frac{d\omega_a}{dt} - \omega_b\omega_c(B - C) = -\frac{3}{r^3}\beta\gamma(B - C),$$

$$B\frac{d\omega_b}{dt} - \omega_c\omega_a(C - A) = -\frac{3}{r^3}\gamma\alpha(C - A),$$ (1)

$$C\frac{d\omega_c}{dt} - \omega_a\omega_b(A - B) = -\frac{3}{r^3}\alpha\beta(A - B).$$

The direction cosines defined in Appendix C are

$$\alpha = \cos(\theta - f)\cos\psi - \sin(\theta - f)\cos\varphi\sin\psi$$

$$\beta = -\cos(\theta - f)\sin\psi - \sin(\theta - f)\cos\varphi\cos\psi$$ (3)

$$\gamma = \sin(\theta - f)\sin\varphi$$

and the angular velocities about the body axes in Euler coordinates as derived in Appendix B are

$$\omega_a = \dot{\theta}\sin\varphi\sin\psi + \dot{\varphi}\cos\psi$$

$$\omega_b = \dot{\theta}\sin\varphi\cos\psi - \dot{\varphi}\sin\psi$$

$$\omega_c = \dot{\theta}\cos\varphi + \dot{\psi}$$ (2)

as given in Section II.

Differentiating equation (2) with respect to time yields

$$\dot{\omega}_a = \ddot{\theta} \sin \varphi \sin \psi + \dot{\theta}\dot{\varphi} \cos \varphi \sin \psi + \dot{\theta}\dot{\psi} \sin \varphi \cos \psi + \ddot{\varphi} \cos \psi - \dot{\varphi}\dot{\psi} \sin \psi$$

$$\dot{\omega}_b = \ddot{\theta} \sin \varphi \cos \psi + \dot{\theta}\dot{\varphi} \cos \varphi \cos \psi - \dot{\theta}\dot{\psi} \sin \varphi \sin \psi - \ddot{\varphi} \sin \psi - \dot{\varphi}\dot{\psi} \cos \psi$$

$$\dot{\omega}_c = \ddot{\theta} \cos \varphi - \dot{\theta}\dot{\varphi} \sin \varphi + \ddot{\psi}.$$

Then substituting the above into (1)

$$\ddot{\theta} \sin \varphi \sin \psi + \ddot{\varphi} \cos \psi = k_1$$
$$\ddot{\theta} \sin \varphi \cos \psi - \ddot{\varphi} \sin \psi = k_2$$
$$\ddot{\theta} \cos \varphi + \ddot{\psi} = k_3$$

where

$$k_1 \equiv (\omega_b \omega_c - \frac{3}{r^3}\beta\gamma)\frac{B-C}{A} - \dot{\theta}\dot{\varphi} \cos \varphi \sin \psi - \dot{\theta}\dot{\psi} \sin \varphi \cos \psi + \dot{\varphi}\dot{\psi} \sin \psi$$

$$k_2 \equiv (\omega_c \omega_a - \frac{3}{r^3}\gamma\alpha)\frac{C-A}{B} - \dot{\theta}\dot{\varphi} \cos \varphi \cos \psi + \dot{\theta}\dot{\psi} \sin \varphi \sin \psi + \dot{\varphi}\dot{\psi} \cos \psi$$

$$k_3 \equiv (\omega_a \omega_b - \frac{3}{r^3}\alpha\beta)\frac{A-B}{C} + \dot{\theta}\dot{\varphi} \sin \varphi.$$

These are the equations of motion for the spin-orbit coupling model defined in Section II. If a rotation state is known, only the three angular accelerations are unknown and these equations can be solved to give

$$\ddot{\theta} = \frac{k_1 \sin \psi + k_2 \cos \psi}{\sin \varphi}$$

$$\ddot{\varphi} = k_1 \cos \psi - k_2 \sin \psi$$

$$\ddot{\psi} = k_3 - \ddot{\theta} \cos \varphi.$$

In this form, the singularity of these equations mentioned in Section II is obvious. Whenever $\sin \varphi = 0$, these solutions are not defined. Of course a solution still exists, it is just impossible to express it in these coordinates. This is why an alternate set, the Wisdom coordinates, were also defined in Section II. The equations of motion in Wisdom

coordinates are derived in exactly the same manner and the solutions are analogous to those above. The transformation from the Euler coordinate system to the Wisdom coordinate system is derived in Appendix F.

APPENDIX E
Determination of Hyperion's position in its orbit

As explained in Section II, it is necessary to know the position of Hyperion in its orbit. One of the state variables defining the initial condition is the true anomaly, related to the time of the observation. Utilizing the knowledge of Hyperion's orbit from the *Explanatory Supplement to the Astronomical Ephemeris and the American Ephemeris and Nautical Almanac,* it is possible to calculate accurately the position of Hyperion in its orbit based on the time of the observation.

The mean anomaly, l, is found from the following relation

$$l = 176°.293 + n(JD - 2415020.0) + 9°.092\sin\sigma + 0°.211\sin(x + \sigma)$$
$$+ 0°.092\sin(x - \sigma) - 0°.077\sin x$$

where JD is the Julian Date, n is the tropical mean daily motion, $n = 16°.9199896$, and the two periodic terms are defined as

$$\sigma = 93°.13 + 0°.562039(JD - 2415020.0)$$
$$x = 148°.72 - 19°.184t$$

where t is the time measured in tropical years from 1900.0. The long-period variable, x, is called ϖ in the *Explanatory Supplement* but I chose to use x to avoid confusion between this variable and the longitude of perihelion, $\varpi \equiv \omega + \Omega$. The longitude of perihelion (called Π in the *Explanatory Supplement*) is given by

$$\varpi = 70°.05 - 18°.6562t - 13°.67\sin x + 0°.93\sin 2x - 0°.47\sin\sigma.$$

From the definition of mean longitude, the mean anomaly is $M = l - \varpi$. The mean anomaly specifies the position of Hyperion in its orbit, but the variable used in the analysis (see Sections II and V) is the true anomaly. The true anomaly, f, can be found if the eccentric anomaly, E, is known. The eccentric anomaly can be found from solving Kepler's equation. For this, the eccentricity must also be known and is calculated using

$$e = 0°.10419 + 0°.02414\cos x - 0°.00401\cos\sigma - 0°.00183\cos 2x.$$

Solving Kepler's equation is an iterative process. I used the form

$$E_{k+1} = E_k + \frac{M - M_k}{1 - e\cos E_k}$$

$$M_k = E_k - e\sin E_k$$

with an initial choice of the eccentric anomaly as

$$E_0 = M + \frac{e\sin M}{1 - \sin(M + e) + \sin M}.$$

Finally, to convert the eccentric anomaly to the true anomaly,

$$\tan\frac{f}{2} = \sqrt{\frac{1 + e}{1 - e}}\, \tan\frac{E}{2}.$$

This identity has the advantage that f/2 and E/2 are always in the same quadrant.

If desired, Hyperion's other orbital elements can be calculated in a similar manner. The goal of this appendix, however, is to show how the light-corrected time of an observation can be converted to a true anomaly corresponding to Hyperion's position in its orbit. As a check to this procedure, I compared the calculated values of the orbital elements to the tabulated values in the 1987 *Astronomical Almanac*. The calculated values were in general agreement with linear interpolated values from the tables. I used the calculated values because they are more accurate.

APPENDIX F
Projected Area of an Ellipsoid

It is necessary to know the projected area of an ellipsoid to compare the model with my lightcurve. The equations of motion for an ellipsoid in the Hyperion-Saturn system were introduced in Section II and developed in Appendix D. These equations determine the dynamics of the system at all times for a given set of initial conditions or rotation state. The dynamics must then be converted to the observable magnitude for comparison to my data. If the area is known, the relative magnitude is $m = -2.5 \log A$ as shown in Section V. Thus, if the projected area of an ellipsoid can be derived from the state variables, the relative magnitude can be calculated and compared with the lightcurve.

The method of finding the projected area will be to convert the equation of an ellipsoid in the body axes

$$1 = \frac{x'^2}{a^2} + \frac{y'^2}{b^2} + \frac{z'^2}{c^2}$$

to the appropriate equation in the Saturnocentric axes and then to compute the area of the resulting projection. Using the transformation matrix derived in Appendix A, this equation can be expressed in terms of the Saturnocentric axes. Using $\vec{X}' = \mathbf{A}^T \vec{X}$, in which the transformation matrix is defined in Appendix A, the body axes can be expressed as

$x' = (\cos\theta\cos\psi - \sin\theta\cos\varphi\sin\psi)x + (\sin\theta\cos\psi + \cos\theta\cos\varphi\sin\psi)y + (\sin\varphi\sin\psi)z$

$y' = (-\cos\theta\sin\psi - \sin\theta\cos\varphi\cos\psi)x - (\sin\theta\sin\psi + \cos\theta\cos\varphi\cos\psi)y + (\sin\varphi\cos\psi)z$

$z' = (\sin\theta\sin\varphi)x - (\cos\theta\sin\varphi)y + (\cos\varphi)z.$

Squaring these equations and substituting it into the equation of the ellipsoid produces an equation of the form

$$1 = Ax^2 + 2Bxy + 2Cxz + Dy^2 + Ez^2 + 2Fyz$$

where

$$A \equiv \frac{\cos^2 \theta \cos^2 \psi + \sin^2 \theta \cos^2 \varphi \sin^2 \psi - 2\cos \theta \sin \theta \cos \varphi \cos \psi \sin \psi}{a^2} +$$

$$\frac{\cos^2 \theta \sin^2 \psi + \sin^2 \theta \cos^2 \varphi \cos^2 \psi + 2\cos \theta \sin \theta \cos \varphi \cos \psi \sin \psi}{b^2} + \frac{\sin^2 \theta \sin^2 \varphi}{c^2}$$

$$B \equiv \frac{\cos \theta \sin \theta \cos^2 \psi - \sin^2 \theta \cos \varphi \cos \psi \sin \psi - \cos^2 \theta \cos \varphi \cos \psi \sin \psi - \cos \theta \sin \theta \cos^2 \varphi \sin^2 \psi}{a^2} +$$

$$\frac{\cos \theta \sin \theta \sin^2 \psi + \sin^2 \theta \cos \varphi \cos \psi \sin \psi - \cos \theta \sin \theta \cos^2 \varphi \cos^2 \psi}{b^2} + \frac{-\cos \theta \sin \theta \sin^2 \varphi}{c^2}$$

$$C \equiv \frac{\cos \theta \sin \varphi \cos \psi \sin \psi - \sin \theta \cos \varphi \sin \varphi \sin^2 \psi}{a^2} +$$

$$\frac{-\cos \theta \sin \varphi \cos \psi \sin \psi - \sin \theta \cos \varphi \sin \varphi \cos^2 \psi}{b^2} + \frac{\sin \theta \cos \varphi \sin \varphi}{c^2}$$

$$D \equiv \frac{\sin^2 \theta \cos^2 \psi + \cos^2 \theta \cos^2 \varphi \sin^2 \psi + 2\cos \theta \sin \theta \cos \varphi \cos \psi \sin \psi}{a^2} +$$

$$\frac{\sin^2 \theta \sin^2 \psi + \cos^2 \theta \cos^2 \varphi \cos^2 \psi - 2\cos \theta \sin \theta \cos \varphi \cos \psi \sin \psi}{b^2} + \frac{\cos^2 \theta \sin^2 \varphi}{c^2}$$

$$E \equiv \frac{\sin^2 \varphi \sin^2 \psi}{a^2} + \frac{\sin^2 \varphi \cos^2 \psi}{b^2} + \frac{\cos^2 \varphi}{c^2}$$

$$F \equiv \frac{\sin \theta \sin \varphi \cos \psi \sin \psi + \cos \theta \cos \varphi \sin \varphi \sin^2 \psi}{a^2} +$$

$$\frac{-\sin \theta \sin \varphi \cos \psi \sin \psi + \cos \theta \cos \varphi \sin \varphi \sin^2 \psi}{b^2} + \frac{-\cos \theta \cos \varphi \sin \varphi}{c^2}.$$

Differentiating this equation with respect to x will give an equation for the projection on the y-z plane, which is the plane perpendicular to the planet to satellite radius vector. Differentiating with respect to x yields

$$0 = 2Ax + 2By + 2Cz$$
$$\Rightarrow x = -\frac{By + Cz}{A}.$$

This can be substituted back into the original equation to obtain the relation

$$1 = Gy^2 + 2Jyz + Hz^2$$

where

$$G \equiv D - \frac{B^2}{A}$$
$$H \equiv E - \frac{C^2}{A}$$
$$J \equiv F - \frac{BC}{A}$$

which is the equation for the projected curve of the ellipsoid as viewed from Saturn. This is also an alternate form for the equation of an ellipse if $4(J^2 - GH) < 0$ (Thomas and Finney 1980). This condition was checked in the programs I wrote to calculate the projected area, and found to be true. Thus, the projected area of an ellipsoid is an ellipse.

The angle of rotation of this ellipse is

$$\delta = \frac{1}{2} \tan^{-1}\left(\frac{2J}{G - H}\right)$$

which can be derived by expressing the equation of the ellipse in polar coordinates and finding the angle corresponding to maximum distance from the center. For polar coordinates

$$\tan \delta = \frac{z}{y}$$
$$r^2 = y^2 + z^2$$

the above equation for an ellipse becomes

$$r^2 = \frac{1 + \tan^2 \delta}{G + H \tan^2 \delta + 2J \tan \delta}.$$

Differentiating this with respect to δ and setting it equal to zero to maximize r yields the solution above.

The area of an ellipse is $A = \pi ab$ where a and b are the semimajor and semiminor axes. In this case,

$$A = \pi r(\delta) r\left(\delta + \frac{\pi}{2}\right)$$

where r is defined above. Since r is a function of the original state variables, the projected area can now be calculated with a knowledge of the dynamics.

As outlined in Section V, two additional rotations must be invoked to calculated the projected area as seen from Earth. The above derivation finds the relationship between the dynamical state variables and the projected area as seen from Saturn. The correction to a geocentric coordinate system is minor. Instead of using the transformation matrix defined in Appendix A, the two additional rotations must be included as

$$\mathbf{A'}^T = \mathbf{BCDEF} = \mathbf{A}^T \mathbf{EF}$$

where

$$\mathbf{E} = \begin{bmatrix} \cos \xi & \sin \xi & 0 \\ -\sin \xi & \cos \xi & 0 \\ 0 & 0 & 1 \end{bmatrix}$$

$$\mathbf{F} = \begin{bmatrix} \cos B & 0 & -\sin B \\ 0 & 1 & 0 \\ \sin B & 0 & \cos B \end{bmatrix}.$$

As defined in Section V, the angle ξ is the true anomaly plus the projection of the angle between the vector pointing to earth and the vector pointing to periapse on the ecliptic. The angle B is the declination of the Earth as seen from Saturn or Hyperion.

The derivation of the projected area as seen from Earth then proceeds in exactly the same manner to produce equations of the same form as above, differing only in how G, H, and J are defined. Thus, in deriving the equation of the projected area of Hyperion as seen from Saturn, I also derived the projected area of Hyperion as seen from Earth.

APPENDIX G
Conversion of Coordinate Systems

The equations of motion have a singularity when $\sin \varphi = 0$, in Euler coordinates (see Appendix D). Since these equations must be solved for a tumbling ellipsoid, it is inevitable that this condition will be approached and another set of coordinates must be used. The other set of coordinates, introduced by Wisdom *et al.* (1984), are defined in Section V and Appendix A. This appendix will detail the procedures used to convert from one set of coordinates to the other.

Since both the Euler angles and Wisdom angles are describing the same position of the ellipsoid in space, it follows that $\mathbf{A} = \mathbf{A}^w$. These matrices are given in Appendix A. As an example, if the Euler angles are known, equating the first and last elements in the bottom rows of the matrices produces the two relations

$$- \cos \varphi^w \sin \psi^w = \sin \varphi \sin \psi$$
$$\cos \varphi^w \cos \psi^w = \cos \varphi$$

so that

$$\tan \psi^w = \frac{\sin \varphi \sin \psi}{\cos \varphi}.$$

There is no ambiguity as to what quadrant the tangent belongs since the sign of the numerator and the denominator are both known. For this appendix, the Wisdom coordinates have a superscript "w" and the Euler coordinates do not. In a similar manner,

$$\tan \varphi^w = \frac{\sin \varphi \cos \psi}{(\cos \varphi / \cos \psi^w)}$$
$$\tan \theta^w = \frac{\cos \theta \sin \psi + \sin \theta \cos \varphi \cos \psi}{- \sin \theta \sin \psi + \cos \theta \cos \varphi \cos \psi}$$

for the other two angles.

The conversion of the velocity components is done in a similar manner. Since the velocity vector is independent of the coordinate system representation, $\vec{\omega} = \vec{\omega}^w$. The components of these vectors are given in Appendix B. Again, assume the Euler

coordinates are known. Then, solving for the Wisdom coordinates gives

$$\dot{\theta}^w = \frac{c_3 \cos \psi - c_1 \sin \psi}{\cos \varphi}$$

$$\dot{\varphi}^w = c_3 \sin \psi + c_1 \cos \psi$$

$$\dot{\psi}^w = c_2 - \dot{\theta}^w \sin \varphi^w$$

where

$$c_1 = \dot{\theta} \sin \varphi \sin \psi + \dot{\varphi} \cos \psi$$

$$c_2 = \dot{\theta} \sin \varphi \cos \psi - \dot{\varphi} \sin \psi$$

$$c_3 = \dot{\theta} \cos \varphi + \dot{\psi}.$$

The procedure to convert Wisdom coordinates to Euler coordinates is analogous and gives similar results.